bioRχiv

An *in vitro* human vessel model to study *Neisseria meningitidis* colonization and vascular damages

Léa Pinon[1], Mélanie Chabaud[2‡], Pierre Nivoit[1‡], Jérôme Wong-Ng[2‡], Tri Tho Nguyen[2], Vanessa Paul[1], Charlotte Bouquerel[2], Sylvie Goussard[1], Pauline Smilovici[1], Emmanuel Frachon[2], Dorian Obino[1], Samy Gobaa[2✉], and Guillaume Duménil[1✉]

[1]Institut Pasteur, Université Paris Cité, INSERM UMR1225, Pathogenesis of vascular infections, F-75015 Paris, France
[2]Institut Pasteur, Université Paris Cité, Biomaterials and Microfluidics core facility, F-75015 Paris, France

Systemic infections leading to sepsis are life-threatening conditions that remain difficult to treat, and the limitations of current experimental models hamper the development of innovative therapies. Animal models are constrained by species-specific differences, while 2D cell culture systems fail to capture the complex pathophysiology of infection. To overcome these limitations, we developed a laser photoablation-based, three-dimensional microfluidic model of meningococcal vascular colonization, a human-specific bacterium that causes sepsis and meningitis. Laser photoablation-based hydrogel engineering allows the reproduction of vascular networks that are major infection target sites, and this model provides the relevant microenvironment reproducing the physiological endothelial integrity and permeability *in vitro*. By comparing with a human-skin xenograft mouse model, we show that the model system not only replicates *in vivo* key features of the infection, but also enables quantitative assessment with a higher spatiotemporal resolution of bacterial microcolony growth, endothelial cytoskeleton rearrangement, vascular E-selectin expression, and neutrophil response upon infection. Our device thus provides a robust solution bridging the gap between animal and 2D cellular models, paving the way for a better understanding of disease progression and developing innovative therapeutics.

Vessel-on-Chip | *Neisseria meningitidis* | Systemic infection | Skin xenograft mouse model | Neutrophils

Correspondence: ***samy.gobaa@pasteur.fr & guillaume.dumenil @pasteur.fr***

‡ ***These authors contributed equally to this work***

Introduction

Infectious diseases remain a significant global health burden, underscoring the need for continued advances in diagnosis, prevention, and treatment strategies. Developing novel therapeutic strategies against infections requires a deep understanding of the underlying physiopathological mechanisms and robust experimental models that capture their hallmark features. The lack of models replicating the 3D infection environment while enabling quantitative assessments is slowing the pace of infection research. Overcoming this limitation is thus essential to drive progress in infectious disease research and address the growing challenge of antimicrobial resistance (1). In this study, we focused on meningococcal disease, which is a model system for systemic infectious diseases that are particularly severe forms of infection. Furthermore, as for most pathogens, meningococcal disease is highly human-specific thus raising specific challenges for the development of experimental models.

Clinical studies have provided the key elements of *N. meningitidis* pathogenesis leading to the vascular damages observed during *purpura fulminans*. Histological studies of postmortem samples have shown that bacteria are found primarily inside blood vessels of different organs, including the liver, the brain, the kidneys, and the skin (2). Bacteria are typically found either associated with the endothelium on the luminal side in tight aggregates (3). The infection is associated with signs of vascular function perturbations, including congestion, intravascular coagulation, and loss of vascular integrity (4). The presence of bacteria within the lumen of blood vessels is also associated with an inflammatory infiltrate, mainly composed of neutrophils and monocytes (5). A valid model of meningococcal infection should thus reproduce the interaction of bacteria with the endothelium and immune cells, as well as infection-induced vascular damage.

To overcome the human-species specificity of meningococcal infections in an animal model, a human skin xenograft mouse model was developed (6). This model was instrumental in demonstrating the importance of bacterial type IV pili (T4P) for vascular colonization (6) and neutrophil recruitment in infected venules (7). The neutrophils interacting with the infected human endothelium are of murine origin, adding complexity to the interpretation of these interactions and the resulting immune response. In addition, while providing the proper tissue con-

text for meningococcal infection, this model is dependent on access to human skin, complex surgical procedures, and animal use.

Another popular experimental approach involves the use of endothelial cells in *in vitro* culture where interaction between *N. meningitidis* and single human cells are studied on flat 2D surfaces (8–11). Such models have been used to decipher the molecular interplay underlying bacteria-bacteria and bacteria-endothelial cell interactions and have been essential in characterizing the host cell reorganization upon bacterial adhesion (12, 13). This notably includes the remodeling of the plasma membrane with the formation of filopodia-shaped protrusions that stabilize the microcolony in the presence of flow-induced shear stress (14). The actin cytoskeleton has been also shown to be highly reorganized underneath bacterial microcolonies, forming a structure reminiscent of a honeycomb, also called cortical plaque (12, 15). Although easy to use, 2D models do not recapitulate the geometry of the vascular system, the proper molecular signaling of inflammation, or the vesicular transport of proteins, all found in a 3D microenvironment (16, 17). An *in vitro* model of meningococcal infections that recapitulates these features in a biologically relevant 3D environment is still lacking.

Producing synthetic yet functional human vasculature has been a dynamic field of research over the last decade, including establishing a 3D vascular system inside a hydrogel loaded onto a microfluidic chip. Endothelial cells are embedded into hydrogels (e.g. fibrin) to self-assemble into interconnected tubes (18–21). Although delivering functional vasculature, this method does not allow for control of the produced vascular geometry. Other methods consist of loading cells into pre-formed structures using molding (22, 23), or viscous fingering (24). These approaches allow the formation of large patterns (120-150 µm) and straight structures, but vessels in tissues are tortuous, ramified, and can be as narrow as 10 µm in diameter. An alternative way for the production of synthetic vasculatures takes advantage of the photoablation technique (25–27). This technique comes with several advantages, including compatibility with a wide range of hydrogels and maximal control over the produced geometry.

In this study, we used a homemade laser ablation setup to engineer a vascular system on-chip with tunable parameters to generate vessels of various shapes and sizes, hence reflecting the complexity of the *in vivo* vascular system. We were able to reproduce *Neisseria meningitidis* vascular colonization *in vitro*. Our Vessel-on-Chip model allowed simulation of the *in vivo* environment during the onset of meningococcal infection with higher spatiotemporal resolution using multidimensional time-lapse imaging while respecting the human-specificity of the meningococcal infection. It replicates key features of the infection, including bacterial adhesion, cellular remodeling, vascular damage, and neutrophil response in infected vessels. The human skin xenograft animal model of meningococcal intravascular infection served as the gold standard to validate our Vessel-on-Chip system. This platform offers a robust bridge to animal and 2D models, providing a physiologically relevant and quantitative 3D tool for studying host-pathogen interactions *in vitro*.

Results

Replicating the geometries of infected vessels using photoablation. *N. meningitidis* infects various types of blood vessels in human cases and in the skin xenograft mouse model (Fig. S1A), including arterioles, venules, and capillaries, which typically range from 10 to 100 µm in diameter, with an average size of 40-60 µm (7). Furthermore, infected vessels are typically branched and exhibit diverse geometries (Fig. 1A). Thus, to study *N. meningitidis* vascular colonization and subsequent vascular damage in relevant vascular geometries, we developed a Vessel-on-Chip (VoC) model using photoablation to allow for complex geometries (26). The chip features a central channel connected to two larger lateral channels and filled with collagen I-type gel, which acts as an extracellular matrix (24). The photoablation process involves carving the collagen I matrix at the center of the microfluidic chip with a focused UV-Laser beam (Fig. 1B), which was tuned to control vessel dimensions (Fig. S1B). Briefly, the chosen design is digitalized into a list of positions to ablate. A pulsed UV-LASER beam is injected into the microscope and shaped to cover the back aperture of the objective. The laser is then focused on each position that needs ablation. After introducing endothelial cells (HUVEC) in the carved regions, formed a vascular lumen by adhering to the substrate (Fig. 1C) and deforming the initially-squared structure (Fig. S1C). The lateral channels remain open to ensure regular liquid flows for nutrient replenishment and the later introduction of bacteria and immune cells.

In vivo, the extracellular matrix is crucial for providing structural and organizational stability (28, 29) thus warranting optimization in our VoC. Endothelial cells intensively sprouted at collagen concentrations of 2.4 mg/ml, (Fig. S1D and 1E), a phenomenon we sought to suppress to better align with the physiological conditions *in vivo* (30). Sprouting decreased with increasing collagen concentrations (Fig. S1E and S1F), which correlates with the increase in gel stiffness (Fig. S1G). However, while two different collagen gels (3.5 mg/ml Corning and 2.4 mg/ml Fujifilm) exhibited a comparable elastic modulus (50 Pa), they showed different effects on the number of endothelial cell sprouts. These results suggest that, in our model, endothelial cell sprouting is determined by both the concentration and composition of collagen, which likely vary in terms of cross-linkage and pore size. Based on these findings, we used a minimum of 4 mg/ml collagen gels for the rest of our study.

The introduction of endothelial cells led to the formation of straight hollow tubes with a circular cross-section (Fig. 1D). The system also allowed the replication of more complex 3D structures (Fig. 1E) and geometries of *in vivo*

blood vessels, based on intravital imaging data. For instance, a vascular branching point, observed in a human vessel imaged in the human skin xenograft mouse model (Fig. 1A), was accurately replicated in the VoC (Fig. 1F). The resulting *in vivo*-like structure in the VoC preserved the aspect ratio of the original vascular geometry and could be further visualized at higher microscopy resolutions compared to blood vessels in animal models. In summary, the photoablation technique, when combined with optimized extracellular matrix properties, enables controlling the construction of reproducible on-chip vessels, that closely mimic those targeted by the meningococci *in vivo*.

The vessels in the VoC exhibit permeability levels comparable to those observed *in vivo*. A key feature of meningococcal infections is its association with a loss of vascular permeability (4, 7). Therefore, relevant *in vitro* infection models should allow the observation and quantification of such a loss of vascular integrity. In this study, we assessed vascular permeability in both the VoC and *in vivo* blood vessels of human (skin xenograft mouse model) origin. Given that vascular integrity and permeability are dependent on intercellular junctions, we first visualized these structures in the chips. Two day post seeding, endothelial cells formed thin and uniform junctions, as evidenced by VE-Cadherin (Fig. 2A) and PECAM-1 (Fig. S2A) stainings, confirming the cohesiveness of the engineered vessel. Additionally, we observed that endothelial cells secreted collagen IV (Fig. 2B), a key component of the basement membrane that provides structural support to blood vessels (31).Then, to evaluate vascular integrity functionally, we performed imaging-based permeability assays using fluorescent 150 kDa dextran (Fig. 2C), comparing fluorescence intensities inside and outside the engineered vessels within our VoC. We observed that sprouting vessels (2.4 mg/ml collagen I) exhibited high permeability, whereas those without sprouts (4 mg/ml collagen I) showed low permeability – no leakage was detected for up to 10 minutes, consistent with *in vivo* observations in the human skin xenograft (Fig. 2D). Altogether, these results demonstrate that our VoC forms a stable physical barrier with low permeability, closely mimicking *in vivo* conditions of human blood vessels in the animal model.

Then, as flow-induced shear stress is a key factor that shapes endothelial cell physiology (32), as well as *N. meningitidis* adhesion along the endothelium (2), we ensured that our model recapitulated *in vivo* nuclear morphologies, known as sensors of the blood flow direction (33). By performing Particle image velocimetry (PIV) experiments in anesthetized animals (Fig. S2B), we measured the flow rates in blood vessels (Fig. S2C) and computed the related wall shear stress (Fig. S2D). Considering blood as Newtonian between 25 µm and 100 µm (34), we showed a wall shear stress of 1.57 Pa (15.7 dynes/cm^2) and 0.31 Pa (3.1 dynes/cm^2) in arterioles and venules, respectively – consistent with previous studies (33, 35, 36). Under venule-like flow conditions controlled by a syringe pump (Fig. S2E), the nucleus of endothelial cells aligned along the flow direction (Fig. 2E) and reached both elongation and orientation of *in vivo* features after 24h of flow exposure (Fig. 2F, 2G and S2F). Of note, nucleus orientation and elongation reached a constant value at 24h (Fig. S2G and S2H), suggesting a homogeneous behavior regardless of wall shear stress for long-term of flow exposure. Also, vessel diameter decreased when endothelial cells were subjected to flow, while cell density remained constant across all conditions (Fig. S2I and S2J). Altogether, these results show that our VoC model correctly responds to flow-induced shear stress and recapitulates the physiological features of the animal model in terms of vascular nucleus morphology and permeability levels.

Adhesion of *N. meningitidis* on chip depends on type-4 pili, while geometry-induced shear stress variations have little impact. The developed *in vitro* vessels allowed us to study meningococcal infection in a controlled 3D environment. Bacteria were introduced into the microfluidic device and circulated through the lumen (Fig 3A). Consistent with observations in infected patients and in the human skin xenograft mouse model (6), meningococci were found to attach to the vascular wall within the infected VoC (Fig. 3B). *N. meningitidis*covered the three-dimensional areas of the endothelium and adhesion occurred both in straight and *in vivo*-like structures (Fig. 3B), forming 3D microcolonies of varying sizes, ranging from a few to tens of microns, as observed in the original geometry *in vivo*. Overall, the infected Vessel-on-Chip model replicates meningococcal vascular colonization in a 3D context and enables high-resolution fluorescence microscopy for detailed monitoring of the infection process *in vitro*.

We confirmed the role of type IV pili-mediated adhesion in the VoC model by comparing a wild-type strain (WT) with the type IV pili-deficient *pilD* mutant strain. After 3 hours of infection under flow, we observed that infection of the VoC with the *pilD* mutant strain only contained rare *N. meningitidis* aggregates (Fig. 3C). In contrast, infection with the WT strain resulted in the formation of numerous and large microcolonies on the vascular walls of the VoC (Fig. 3D, S3A and S3B).

We next investigated whether vascular geometry and associated shear stress variations affect *N. meningitidis* adhesion. To this end, we infected vessel-on-chip models of increasing geometrical complexity, circle, diamond, and in vivo-like branched structures, generating distinct wall shear stress profiles (Fig. 3E). Measured wall shear stress ranged from 0.025 to 0.1 Pa (Fig. 3F). The distribution of adherent bacteria as a function of shear stress level (orange curve) closely mirrored the shear stress distribution available in the device (blue curve) indicating no preferential adhesion sites across shear stress gradients. This was confirmed by Spearman correlation analysis, which showed strong correlations between the two means curves ($0.58 < S.\ corr. < 0.83$) (Fig. 3F). These findings

suggest that within this flow range, adhesion is not impacted by geometry-induced shear stress variations, consistently with *in vivo* observations and previous studies (2).

Progression of *N. meningitidis* colonization in the Vessel-on-Chip is similar to *in vivo* observations. In both the VoC and animal model, we observed the fusion of bacterial aggregates (Fig. S4A), highlighting the dynamical properties of bacterial expansion (9, 37). We then challenged the impact of flows in bacterial growth and morphology. Microcolony expansion was thus assessed under flow (0.5 µl/min which corresponds to $\sim$ 0.1 Pa) by monitoring the increase of surface area covered by adherent bacteria over 3 hours of infection, as *in vivo* experiments (Fig. 4A and S4B). Individual microcolonies (shaded curves Fig. 4A), exhibited a mean linear growth trend (solid curve) in both the VoC model and the mouse model. We normalized the quantification of the colony doubling time according to the first time-point where a single bacterium is attached to the vessel wall. Thus, early-adhesion bacteria are defined by a longer curve while late-adhesion bacteria are defined by a shorter curve. We observed that the time required for microcolony expansion in both VoC (with and without flow) and human skin-grafted mice is similar (approximately 20 minutes, Fig. 4B), and is lower than in agar-pad cultures (30-40 minutes (38)). This trend likely reflects a combination of bacterial proliferation, fusion, and subsequent adhesion of circulating bacteria, as previously proposed (39). We then observed that, under flow conditions, bacterial microcolonies were submitted to a morphological change within the VoC (Fig. 4C and 4D). Microcolonies elongated and aligned along the vessel length, corresponding to the direction of flow. Unlike under static conditions, both elongation and orientation properties of bacterial microcolonies in the presence of flow were similar to those found *in vivo*, demonstrating the importance of the flow to recapitulate the proper infection conditions in the VoC. Altogether, these findings demonstrate that our model effectively replicates the key aspects of *N. meningitidis* colonization, including bacterial dynamics, morphology, and functional behavior, closely mirroring the infection process observed *in vivo*.

***N. meningitidis* vascular colonization increases vessel permeability within the Vessel-on-Chip.** Vascular permeability was shown to increase at the late stages of meningococcal infections (24h post-infection), as evidenced in the human skin xenograft mouse model by the accumulation of intravenously injected Evans blue in the surrounding tissues (7). We therefore used a direct permeability assay using a 150 kDa FITC Dextran in both the VoC and the mouse model (Fig. 4E and 4F) to determine the permeability at the early stage of inflammation and infected vessels. Histamine was used as a positive control (40), showing a similar response under inflammatory conditions in both the *in vivo* and VoC models (Fig. 4E and 4F). After 3 hours post-infection, vascular permeability importantly increased in the infected VoC, consistent with findings from previous 2D *in vitro* studies (41–44). In contrast, only a subtle increase in vascular permeability was observed in infected human vessels in the skin xenograft mouse model (Fig. S4C), most likely reflecting the presence of additional cell types surrounding the vessel wall *in vivo*, which enhance barrier integrity at early stages of infection (42). In addition, at later stages of infections, vascular integrity might also be affected by intravascular coagulation induced by meningococci (45). Overall, our results show that, despite moderate differences between the VoC and the animal model in the kinetics of endothelial integrity loss, our VoC offers a suitable model to study the direct consequences, including the increase in vessel permeability, of the host-pathogen interaction between *N. meningitidis* and endothelial cells upon vascular colonization with a high spatiotemporal resolution.

Flow-induced aligned actin stress fibers are reorganized beneath bacterial microcolonies. *N. meningitidis* bacterial microcolonies have been shown to reorganize both the plasma membrane and the actin cytoskeleton upon adhesion at the surface of endothelial cells in 2D models (13, 15, 46). However, *in vivo*, such events are challenging to observe.

Also, endothelial cells experience flow-induced mechanical stresses *in vivo*, which is known to influence the state of the actin cytoskeleton (47, 48). The impact of such actin cytoskeleton rearrangements, potentially impacting bacteria-induced responses, has never been explored. This requires a high resolutive imaging of infection within a perfused 3D environment, that is provided by our system. Thus, within the micro-physiological environment of the Vessel-on-Chip model, we investigated whether similar actin reorganization in endothelial cells occurs upon infection by *N. meningitidis*. We first confirmed that, in the absence of flow, actin stress fibers exhibit random orientations (Fig. 5A and 5B). In contrast, when endothelial cells in the VoC were submitted to flow for 2h, actin stress fibers became highly organized and aligned with the flow direction (Fig. 5A and 5B). Notably, this rapid adaptation was quantitatively confirmed by the significant reduction in the interquartile range (IQR) of fiber orientation when increasing shear stress levels, regardless of the duration (2h or 24h) of flow exposure (Fig. S5A).

Despite the flow-mediated alignment of the actin fibers, bacterial microcolonies adhering at the surface of endothelial cells in the VoC were able to induce the formation of the honeycomb-shaped actin structures underneath bacterial aggregated, similar to observations made in infection in the absence of flow (Fig. 5C and 5D). This specific bacteria-induced reorganization of the actin cytoskeleton, which occurs under flow conditions, mirrors the flow-driven elongated shape of the bacterial microcolonies. After 3 hours of infection, 65% of the microcolonies had formed

the actin cortical plaque below bacterial aggregates, while 35% did not show any visible structure (Fig. 5E), which is close to the 2D experiments (Fig. 5B). The fluorescence intensity of F-actin beneath the microcolonies was twice as high compared to non-infected areas (Fig. 5F), reaching levels previously observed in 2D models (15). The highly organized actin fibers in the VoC were drastically reorganized by the presence of the bacterial microcolonies, as evidenced by the reduction in actin fiber coherency (fiber symmetry) upon infection (Fig. 5G). Noticeably, F-actin fluorescence intensity was correlated with actin fiber coherency (Fig. S5C). Collectively, these results demonstrate that *N. meningitidis* reorganizes the endothelial cell actin cytoskeleton in the VoC under flow conditions, despite the presence of a pre-existing highly organized and aligned F-actin network. This is of particular importance when considering the infection process *in vivo* – during which endothelial cells are submitted to flow-induced wall shear stress – leads to actin fiber alignment and high symmetry prior to bacterial adhesion.

Neutrophils respond to *N. meningitidis* infection similar to in the animal model. The presence of an inflammatory infiltrate, predominantly composed of neutrophils, in the vicinity of infected vessels is another cardinal feature of meningococcal infection (49). Previous *in vivo* studies have demonstrated that *N. meningitidis* infection leads to the recruitment of neutrophils along infected venules, a process driven by the bacteria-mediated upregulation of E-selectin expression at the surface of infected endothelial cells (7). To assess whether this aspect of the infection can be recapitulated within the VoC upon meningococcal infection, we examined E-selectin expression in response to inflammatory stimuli and infection. Endothelial cells did not express E-selectin in the absence of infection (Fig. 6A, S6A and S6B), clearly demonstrating that the experimental setup successfully maintained appropriate basal conditions all along vessel formation. However, both TNFα stimulation and *N. meningitidis* infection led to an important increase in E-selectin expression all over the vessel (Fig. 6A, S6A and S6B). This is due to both the increase of the number of E-selectin^{+}-activated cells (Fig. 6B), and the massive upregulation of E-selectin expression of these activated cells (Fig. 6C) at the single-cell level. Interestingly, infection with the non-piliated *pilD* mutant strain induced E-selectin expression to a much lesser extent when compared to the wild-type strain, highlighting the role of bacterial adhesion in this process (Fig. 6A and S6C). The expression of E-selectin on *N. meningitidis*-infected endothelium was more spatially heterogeneous than on the TNFα-inflamed one (Fig. S6A and S6B), suggesting a spatial cell-to-cell heterogeneity in endothelial cell response upon infection, which correlates with *in vivo* observations (7).
We next assessed the local recruitment of neutrophils to infected on-chip model. To this end, human neutrophils were purified from the blood of healthy donors and perfused under flow conditions in the microfluidic chip (Fig. 6D). Figures 6E and 6F show the increase in the numbers of neutrophils attaching to the VoC wall upon inflammatory stimulation, whether with TNFα or *N. meningitidis*-induced intravascular colonization, compared to control conditions, consistent with *in vivo* recruitment of neutrophils to infected vessels (6). We also observed phagocytosis of bacteria by human neutrophils (Fig. 6E), comparable to those observed in the humanized mouse model (7). In addition, we could observed the typical cascade of human neutrophil adhesion events, including rolling, arrest, and crawling on the endothelial surface (Fig. S6D and S6E), as previously described (50). Altogether, these results demonstrate that we have successfully recapitulated the full spectrum of human immune-endothelial cell interactions, from the adhesion cascade to the neutrophil recruitment and phagocytosis at infection sites, demonstrating that our VoC is suitable for the study of the immune response during *N. meningitidis* infection. Furthermore, in contrast to the humanized mouse model which is limited by the interactions of murine immune cells with human infected endothelial cells, our Vessel-on-Chip model has the potential to fully capture the human neutrophil response during vascular infections, in a species-matched microenvironment.

Discussion

In this work, we have developed an *in vitro* 3D human Vessel-on-Chip microfluidic-based platform that accurately mimics the vascular environment encountered by *N. meningitidis* during intravascular colonization. We not only characterized our model from the microfabrication to the cellular response under infection conditions, but we also demonstrated that our VoC strongly replicates key aspects of the *in vivo* human skin xenograft mouse model, the gold standard for studying meningococcal disease under physiological conditions. The *N. meningitidis*-infected VoC offers several distinct advantages described below, bridging the current gap between 2D *in vitro* and animal models for studying vascular infections.
The first advantage of our model is its ability to replicate complex *in vivo*-like vessel geometries. Although photoablation is often considered practically slow (21), our optimized process enables fast replication of complex geometries, thus facilitating the preparation of tens of devices in an hour. The speed capabilities drastically improve with the pulsing repetition rate. Given that our laser source emits pulses at 10kHz, as compared to other photoablation lasers with repetitions around 100 Hz, our solution could potentially gain a factor of 100 in ablation speed. Also, we precisely controlled the size and shape of the UV-carved hydrogel scaffolds, enabling the replication of tissue-engineered VoC structures derived from intravital images, including straight, branched, and tortuous configurations. Vascular geometries, known to disturb streamlines and wall shear stress (48), have been implicated in the initial formation of atherosclerosis (51) and may also

contribute to bacterial colonization in regions of low velocity (32). Our tunable system thus represents a unique tool to further explore how vascular geometries and shear stress impact vascular colonization in different conditions.

A second significant advantage of our VoC is the replication of endothelial tissue in an *in vivo*-like physiological state. This includes vessels of low permeability, with well-defined intercellular junctions, and able to dynamically maintain their integrity. The possibility to perfuse the microfluidic chips enables to induce of a flow-mediated wall shear stress, leading to the reorientation of actin fibers and the elongation of nuclei, similar to what we observed in the *in vivo* conditions. These findings demonstrate that our system successfully replicates the *in vivo* conditions of endothelial cells, emphasizing the physiological relevance of our approach and creating a realistic *in vitro* microenvironment to study *N. meningitidis* vascular infection.

In the Vessel-on-Chip, the colonization of *N. meningitidis* increases vessel permeability, also aligning with expectations from previous *in vitro* studies (41–43). *In vivo*, such an increase in permeability is only subtly visible after a few hours of infection but typically manifests at later stages (around 24 hours post-infection (7)). This difference is most likely associated with the presence of other cell types (e.g., fibroblasts, pericytes, perivascular macrophages) in the *in vivo* tissues and the onset of intravascular coagulation (45, 52). Coagulation has recently been successfully recapitulated in 3D vascular models under healthy conditions (53), suggesting that our system could also be used to study the later stages of infection and the associated coagulation process.

Likewise, while perivascular cells and fibroblasts have been extensively studied in *in vitro* models (16, 54), their influence on *N. meningitidis*/host interactions have not been explored and our set-up would permit this type of studies. Recent studies show that substrate stiffness, through tissue remodeling, can affect bacterial adhesion (55) and uptake (56). We hypothesize that fibroblasts, by remodeling the ECM (57), and perivascular cells, by enhancing mechanical stability and secreting the basement membrane (58), can alter vascular tissue and thus locally influence *N. meningitidis*-endothelium interactions, which can have larger consequences during vascular infection. Therefore, integrating perivascular cells, along with other microvascular cell types, into the physiological microenvironment of our model is crucial to understanding their role in host-pathogen interactions.

The infected Vessel-on-Chip model also replicates the dynamics, morphology, and dependency of T4P for efficient intravascular colonization. *N. meningitidis* introduced in the VoC readily adheres along the endothelium and forms three-dimensional microcolonies that increase in size and at a rate comparable to *in vivo* conditions. The microcolony shift in morphology we observed between no-flow and flow conditions is likely a consequence of the influence of shear stress on these viscoelastic structures (9, 59, 60). While geometry-induced shear stress gradients did not strongly impact *N. meningitidis* adhesion, flow could have significant implications for the dynamics of vascular colonization by spreading adherent meningococcal microcolonies along the endothelium. Following their initial T4P-mediated adhesion at the surface of endothelial cells, meningococci subsequently reorganize the actin cytoskeleton within the on-chip model, leading to the formation of the typical honeycomb-shaped cortical plaque (12, 15). This shed light on the capacity of *N. meningitidis* to reorient the initially organized, parallel actin network in the 3D microenvironment and underscore its importance for colony stabilization, as observed in 2D and *in vivo* (14, 37).

Finally, our model recapitulates the microenvironment required to study the human neutrophil response in contact with infected human endothelial cells. Unlike the humanized skin xenograft mouse model that involves heterotypic interactions between murine neutrophils and human endothelium (7), the VoC model allows for species-matched interactions between purified human neutrophils and human endothelial cells. While in basal conditions no sign of inflammation was detected, *N. meningitidis* infection led to the upregulation of E-selectin on the endothelial surface and the increase of neutrophil adhesion on the vascular wall, leading to bacterial phagocytosis. These behaviors, including rolling, crawling, and active phagocytosis of adherent *N. meningitidis*, closely mirror immune responses observed *in vivo* (7). In addition, we observed that the *pilD* mutant strain, which lacks T4P, triggers a milder E-selectin upregulation, indicating that T4P-mediated adhesion plays a significant role in endothelial cell activation, thereby enhancing the subsequent neutrophil adhesion. The VoC model also facilitates quantitative measurements of key parameters, as illustrated by our ability to finely assess vessel permeability or detect E-selectin upregulation at the single-cell level, capturing both the number and intensity of individual activated cells. Reaching such a level of detail is often challenging in animal models because of geometric and resolution limitations, thus our system represents a suitable alternative to facilitate both the observations and the quantification. Furthermore, other immune cells respond to *N. meningitis* and their role can be explored using our model. For instance, macrophages are activated upon *N. meningitis* infection, eliminate the bacteria through phagocytosis, and produce pro-inflammatory cytokines and chemokines to activate other immune cells (61). Also, dendritic cells, which phagocytose *N. meningitidis*, further activate adaptative response through immune synapse formation with T cells (61). Such an immune response, yet complex, would be interesting to study in our model as skin-xenograft mice are deprived of B and T lymphocytes to ensure accepting human skin grafts.

To conclude, our Vessel-on-Chip system, which leverages 3D-engineered microenvironments, represents a significant advancement in studying bacterial physiology and pathology in realistic infection contexts. We have demonstrated that our model provides a 3D *in vitro* platform that

recapitulates *N. meningitidis* vascular adhesion and microcolony formation within complex vascular morphologies, as well as the subsequent pathological consequences. Although the system was optimized for meningococcal infection, and given that the vasculature serves as a primary route for systemic infections (52, 62) and bacterial dissemination to various organs (63, 64), our approach paves the way for investigating the pathophysiological mechanisms triggered by other pathogens responsible for systemic infections (11) (e.g., bacteria, viruses, fungi) in different vascular systems (e.g., capillary beds, arteries) (65). It is also suitable for both quantitative analysis and applied research in the biophysics and biomedical fields, including drug screening and antibiotic resistance studies. By enabling detailed exploration of previously overlooked aspects of infections (e.g. vascular geometry difference, cell-specificity, virus/fungi/other bacteria), our model has the potential to advance the development of novel therapeutic strategies to better manage intravascular infections.

References

1. J. L. et al. Murray. Global burden of bacterial antimicrobial resistance in 2019: a systematic analysis. *The Lancet*, 399(10325):629–655, 2022.
2. Emilie Mairey, Auguste Genovesio, Emmanuel Donnadieu, Christine Bernard, Francis Jaubert, Elisabeth Pinard, Jacques Seylaz, Jean-Christophe Olivo-Marin, Xavier Nassif, and Guillaume Dumenil. Cerebral microcirculation shear stress levels determine Neisseria meningitidis attachment sites along the blood–brain barrier . *Journal of Experimental Medicine*, 203(8):1939–1950, 07 2006. ISSN 0022-1007. doi: 10.1084/jem.20060482.
3. K Melican and Guilaume Dumenil. Vascular colonization by neisseria meningitidis. *Current Opinion in Microbiology*, 15(1), 2012. doi: 10.1016/j.mib.2011.10.008.
4. Saul N Faust, Robert S Heyderman, and Michael Levin. Disseminated intravascular coagulation and purpura fulminans secondary to infection. *Best Practice & Research Clinical Haematology*, 13(2):179–197, 2000. doi: 10.1053/beha.2000.0067.
5. Jeannette Guarner, Patricia W Greer, Anne Whitney, Wun-Ju Shieh, Marc Fischer, Elizabeth H White, George M Carlone, David S Stephens, Tanja Popovic, and Sherif R Zaki. Pathogenesis and diagnosis of human meningococcal disease using immunohistochemical and pcr assays. *American Journal of Clinical Pathology*, 122(5):754–764, 2004.
6. Keira Melican, Paula Michea Veloso, Tiffany Martin, Patrick Bruneval, and Guillaume Dumenil. Adhesion of neisseria meningitidis to dermal vessels leads to local vascular damage and purpura in a humanized mouse model. *PLOS Pathogens*, 9(1):1–11, 01 2013. doi: 10.1371/journal.ppat.1003139.
7. Valeria Manriquez, Pierre Nivoit, Tomas Urbina, Hebert Echenique-Rivera, Keira Melican, Marie-Paule Fernandez-Gerlinger, Patricia Flamant, Taliah Schmitt, Patrick Bruneval, Dorian Obino, and Guillaume Duménil. Colonization of dermal arterioles by neisseria meningitidis provides a safe haven from neutrophils. *Nature Communications*, 12(1):4547, Jul 2021. ISSN 2041-1723. doi: 10.1038/s41467-021-24797-z.
8. Nicolas Doulet, Emmanuel Donnadieu, Marie-Pierre Laran-Chich, Florence Niedergang, Xavier Nassif, Pierre Olivier Couraud, and Sandrine Bourdoulous. Neisseria meningitidis infection of human endothelial cells interferes with leukocyte transmigration by preventing the formation of endothelial docking structures . *Journal of Cell Biology*, 173(4):627–637, 05 2006. ISSN 0021-9525. doi: 10.1083/jcb.200507128.
9. Daria Bonazzi, Valentina Lo Schiavo, Silke Machata, Ilyas Djafer-Cherif, Pierre Nivoit, Valeria Manriquez, Hirokazu Tanimoto, Julien Husson, Nelly Henry, Hugues Chaté, Raphael Voituriez, and Guillaume Dumenil. Intermittent pili-mediated forces fluidize neisseria meningitidis aggregates promoting vascular colonization. *Cell*, 174(1):143–155.e16, 2018. ISSN 0092-8674. doi: https://doi.org/10.1016/j.cell.2018.04.010.
10. Kevin Denis, Marion Le Bris, Loic Le Guennec, Jean-Philippe Barnier, Camille Faure, Anne Gouge, Haniaa Bouzinba-Ségard, Anne Jamet, Daniel Euphrasie, Beatrice Durel, Nicolas Barois, Philippe Pelissier, Philippe C. Morand, Mathieu Coureuil, Frank Lafont, Olivier Join-Lambert, Xavier Nassif, and Sandrine Bourdoulous. Targeting type iv pili as an antivirulence strategy against invasive meningococcal disease. *Nature Microbiology*, 4(6):972–984, Jun 2019. ISSN 2058-5276. doi: 10.1038/s41564-019-0395-8.
11. Raquel Alonso-Roman, Alexander S. Mosig, Marc Thilo Figge, Kai Papenfort, Christian Eggeling, Felix H. Schacher, Bernhard Hube, and Mark S. Gresnigt. Organ-on-chip models for infectious disease research. *Nature Microbiology*, 4 2024. doi: 10.1038/s41564-024-01645-6.
12. A J Merz and M So. Attachment of piliated, opa- and opc- gonococci and meningococci to epithelial cells elicits cortical actin rearrangements and clustering of tyrosine-phosphorylated proteins. *Infection and Immunity*, 65(10):4341–4349, 1997. doi: 10.1128/iai.65.10.4341-4349.1997.
13. Arthur Charles-Orszag, Feng-Ching Tsai, Daria Bonazzi, Valeria Manriquez, Martin Sachse, Adeline Mallet, Audrey Salles, Keira Melican, Ralitza Staneva, Aurélie Bertin, Corinne Millien, Sylvie Goussard, Pierre Lafaye, Spencer Shorte, Matthieu Piel, Jacomine Krijnse-Locker, Françoise Brochard-Wyart, Patricia Bassereau, and Guillaume Duménil. Adhesion to nanofibers drives cell membrane remodeling through one-dimensional wetting. *Nature Communications*, 9(1):4450, Oct 2018. ISSN 2041-1723. doi: 10.1038/s41467-018-06948-x.
14. Guillain Mikaty, Magali Soyer, Emilie Mairey, Nelly Henry, Dave Dyer, Katrina T. Forest, Philippe Morand, Stéphanie Guadagnini, Marie Christine Prévost, Xavier Nassif, and Guillaume Dumenil. Extracellular bacterial pathogen induces host cell surface reorganization to resist shear stress. *PLOS Pathogens*, 5(2):1–14, 02 2009. doi: 10.1371/journal.ppat.1000314.
15. Magali Soyer, Arthur Charles-Orszag, Thibault Lagache, Silke Machata, Anne-Flore Imhaus, Audrey Dumont, Corinne Millien, Jean-Christophe Olivo-Marin, and Guillaume Dumenil. Early sequence of events triggered by the interaction of eisseria meningitidis with endothelial cells. *Cellular Microbiology*, 16(6):878–895, 2014. doi: https://doi.org/10.1111/cmi.12248.
16. Giovanni S. Offeddu, Kristina Haase, Mark R. Gillrie, Ran Li, Olga Morozova, Dean Hickman, Charles G. Knutson, and Roger D. Kamm. An on-chip model of protein paracellular and transcellular permeability in the microcirculation. *Biomaterials*, 212:115–125, 2019. ISSN 0142-9612. doi: https://doi.org/10.1016/j.biomaterials.2019.05.022.
17. Bo Wang, Ruomeng Chen, Hongqian Gao, Xiaohan Lv, Lifang Chen, Weirong Wang, Yaxiong Liu, Nanbo Zheng, and Rong Lin. A comparative study unraveling the effects of tnf-α stimulation on endothelial cells between 2d and 3d culture. *Biomedical Materials*, 15(6): 065018, sep 2020. doi: 10.1088/1748-605X/ab95e3.
18. Sudong Kim, Hyunjae Lee, Minhwan Chung, and Noo Li Jeon. Engineering of functional, perfusable 3d microvascular networks on a chip. *Lab on a chip*, 13(8):1489—1500, April 2013. ISSN 1473-0197. doi: 10.1039/c3lc41320a.
19. Jihoon Ko, Younggyun Lee, Somin Lee, Seung-Ryeol Lee, and Noo Li Jeon. Human ocular angiogenesis-inspired vascular models on an injection-molded microfluidic chip. *Advanced Healthcare Materials*, 8(15):1900328, 2019. doi: https://doi.org/10.1002/adhm.201900328.
20. Kristina Haase, Giovanni S. Offeddu, Mark R. Gillrie, and Roger D. Kamm. Endothelial regulation of drug transport in a 3d vascularized tumor model. *Advanced Functional Materials*, 30(48):2002444, 2020. doi: https://doi.org/10.1002/adfm.202002444.
21. Colleen O'Connor, Eileen Brady, Ying Zheng, Erika Moore, and Kelly R. Stevens. Engineering the multiscale complexity of vascular networks. *Nature Reviews Materials*, 7(9): 702–716, Sep 2022. ISSN 2058-8437. doi: 10.1038/s41578-022-00447-8.
22. Kristina Haase and Roger D Kamm. Advances in on-chip vascularization. *Regenerative Medicine*, 12(3):285–302, 2017. doi: 10.2217/rme-2016-0152. PMID: 28318376.
23. Claire A Dessalles, Clara Ramón-Lozano, Avin Babataheri, and Abdul I Barakat. Luminal flow actuation generates coupled shear and strain in a microvessel-on-chip. *Biofabrication*, 14(1):015003, oct 2021. doi: 10.1088/1758-5090/ac2baa.
24. Anna Herland, Andries D. van der Meer, Edward A. FitzGerald, Tae-Eun Park, Jelle J. F. Sleeboom, and Donald E. Ingber. Distinct contributions of astrocytes and pericytes to neuroinflammation identified in a 3d human blood-brain barrier on a chip. *PLOS ONE*, 11(3): 1–21, 03 2016. doi: 10.1371/journal.pone.0150360.
25. Offra Sarig-Nadir, Noga Livnat, Ruthy Zajdman, Shy Shoham, and Dror Seliktar. Laser photoablation of guidance microchannels into hydrogels directs cell growth in three dimensions. *Biophysical Journal*, 96(11):4743–4752, 2009. ISSN 0006-3495. doi: https://doi.org/10.1016/j.bpj.2009.03.019.
26. Nathalie Brandenberg and Matthias P. Lutolf. In situ patterning of microfluidic networks in 3d cell-laden hydrogels. *Advanced Materials*, 28(34):7450–7456, 2016. doi: https://doi.org/10.1002/adma.201601099.
27. Alessandro Enrico, Dimitrios Voulgaris, Rebecca Östmans, Naveen Sundaravadivel, Lucille Moutaux, Aurélie Cordier, Frank Niklaus, Anna Herland, and Göran Stemme. 3d microvascularized tissue models by laser-based cavitation molding of collagen. *Advanced Materials*, 34(11):2109823, 2022. doi: https://doi.org/10.1002/adma.202109823.
28. Kristina Haase, Filippo Piatti, Minerva Marcano, Yoojin Shin, Roberta Visone, Alberto Redaelli, Marco Rasponi, and Roger D. Kamm. Physiologic flow-conditioning limits vascular dysfunction in engineered human capillaries. *Biomaterials*, 280:121248, 2022. ISSN 0142-9612. doi: https://doi.org/10.1016/j.biomaterials.2021.121248.
29. George E. Davis and Donald R. Senger. Endothelial extracellular matrix. *Circulation Research*, 97(11):1093–1107, 2005. doi: 10.1161/01.RES.0000191547.64391.e3.
30. Andrew C. Dudley and Arjan W. Griffioen. The modes of angiogenesis: an updated perspective. *Angiogenesis*, 26(4):477–480, Nov 2023. ISSN 1573-7209. doi: 10.1007/s10456-023-09895-4.
31. Claire Leclech, Carlo F. Natale, and Abdul I. Barakat. The basement membrane as a structured surface – role in vascular health and disease. *Journal of Cell Science*, 133(18): jcs239889, 09 2020. ISSN 0021-9533. doi: 10.1242/jcs.239889.
32. Hui Lin Zhou, Xi Zhuo Jiang, and Yiannis Ventikos. Role of blood flow in endothelial functionality: a review. *Frontiers in Cell and Developmental Biology*, 11, 2023. ISSN 2296-634X. doi: 10.3389/fcell.2023.1259280.
33. P. F. Davies. Flow-mediated endothelial mechanotransduction. *Physiological Reviews*, 75 (3):519–560, 1995. doi: 10.1152/physrev.1995.75.3.519. PMID: 7624393.
34. Axel R. Pries, Timothy W. Secomb, and Peter Gaehtgens. Design principles of vascular beds. *Circulation Research*, 77(5):1017–1023, 1995. doi: 10.1161/01.RES.77.5.1017.
35. John N. Osinnski, David N. Ku, Srinivasan Mukundan Jr, Francis Loth, and Roderic I Pettigrew. Determination of wall shear stress in the aorta with the use of mr phase velocity mapping. *Journal of Magnetic Resonance Imaging*, 5(6):640–647, 1995. doi: https://doi.org/10.1002/jmri.1880050605.
36. Zekun Peng, Bingyan Shu, Yurong Zhang, and Miao Wang. Endothelial response to pathophysiological stress. *Arteriosclerosis, Thrombosis, and Vascular Biology*, 39(11):e233–e243, 2019. doi: 10.1161/ATVBAHA.119.312580.
37. Tamara Rossy, Tania Distler, Lucas A. Meirelles, Joern Pezoldt, Jaemin Kim, Lorenzo Talà, Nikolaos Bouklas, Bart Deplancke, and Alexandre Persat. Pseudomonas aeruginosa type iv pili actively induce mucus contraction to form biofilms in tissue-engineered human airways. *PLOS Biology*, 21(8):1–32, 08 2023. doi: 10.1371/journal.pbio.3002209.
38. Dmitry Ershov, Minh-Son Phan, Joanna W. Pylvänäinen, Stéphane U. Rigaud, Laure Le Blanc, Arthur Charles-Orszag, James R. W. Conway, Romain F. Laine, Nathan H. Roy, Daria Bonazzi, Guillaume Duménil, Guillaume Jacquemet, and Jean-Yves Tinevez. Track-

mate 7: integrating state-of-the-art segmentation algorithms into tracking pipelines. *Nature Methods*, 19(7):829–832, Jul 2022. ISSN 1548-7105. doi: 10.1038/s41592-022-01507-1.

39. Emmanuel Eugene, Isabelle Hoffmann, Celine Pujol, Pierre-Olivier Couraud, Sandrine Bourdoulous, and Xavier Nassif. Microvilli-like structures are associated with the internalization of virulent capsulated Neisseria meningitidis into vascular endothelial cells. *Journal of Cell Science*, 115(6):1231–1241, 03 2002. ISSN 0021-9533. doi: 10.1242/jcs.115.6.1231.
40. Gyohei Egawa, Satoshi Nakamizo, Yohei Natsuaki, Hiromi Doi, Yoshiki Miyachi, and Kenji Kabashima. Intravital analysis of vascular permeability in mice using two-photon microscopy. *Scientific Reports*, 3(1):1932, Jun 2013. ISSN 2045-2322. doi: 10.1038/srep01932.
41. Anna Kobsar, Celine Siauw, Stepan Gambaryan, Sabrina Hebling, Christian Speer, Alexandra Schubert-Unkmeir, and Martin Eigenthaler. Neisseria meningitidis induces platelet inhibition and increases vascular endothelial permeability via nitric oxide regulated pathways. *Thromb Haemost*, 106(12):1127–1138, Nov 2017. ISSN 0340-6245. doi: 10.1160/TH11-07-0491.
42. Leo M. Endres, Marvin Jungblut, Mustafa Divyapicigil, Markus Sauer, Christian Stigloher, Myron Christodoulides, Brandon J. Kim, and Alexandra Schubert-Unkmeir. Development of a multicellular in vitro model of the meningeal blood-csf barrier to study neisseria meningitidis infection. *Fluids and Barriers of the CNS*, 19(1):81, Oct 2022. ISSN 2045-8118. doi: 10.1186/s12987-022-00379-z.
43. Alexandra Schubert-Unkmeir, Christian Konrad, Heiko Slanina, Florian Czapek, Sabrina Hebling, and Matthias Frosch. Neisseria meningitidis induces brain microvascular endothelial cell detachment from the matrix and cleavage of occludin: A role for mmp-8. *PLOS Pathogens*, 6(4):1–15, 04 2010. doi: 10.1371/journal.ppat.1000874.
44. Jason Ziveri, Loïc Le Guennec, Isabel dos Santos Souza, Jean-Philipe Barnier, Samuel M. Walter, Youssouf Diallo, Yasmine Smail, Elodie Le Seac'h, Haniaa Bouzinba-Segard, Camille Faure, Philippe C. Morand, Irié Carel, Nicolas Perriere, Taliah Schmitt, Brigitte Izac, Franck Letourneur, Mathieu Coureuil, Thomas Rattei, Xavier Nassif, and Sandrine Bourdoulous. Angiopoietin-like 4 protects against endothelial dysfunction during bacterial sepsis. *Nature Microbiology*, 9:2434–2447, June 2024.
45. Jean-Philippe Corre, Dorian Obino, Pierre Nivoit, Aline Yatim, Taliah Schmitt, and Guillaume Duménil. Anti-thrombotic treatment enhances antibiotic efficiency in a humanized model of meningococcemia. *bioRxiv*, 2022. doi: 10.1101/2022.01.10.475613.
46. Alexey J. Merz, Caroline A. Enns, and Magdalene So. Type iv pili of pathogenic neisseriae elicit cortical plaque formation in epithelial cells. *Molecular Microbiology*, 32(6):1316–1332, 1999. doi: https://doi.org/10.1046/j.1365-2958.1999.01459.x.
47. Adel M. Malek and Seigo Izumo. Mechanism of endothelial cell shape change and cytoskeletal remodeling in response to fluid shear stress. *Journal of Cell Science*, 109(4): 713–726, 04 1996. ISSN 0021-9533. doi: 10.1242/jcs.109.4.713.
48. Peter F. Davies. Hemodynamic shear stress and the endothelium in cardiovascular pathophysiology. *Nature Clinical Practice Cardiovascular Medicine*, 6(1):16–26, Jan 2009. ISSN 1743-4300. doi: 10.1038/ncpcardio1397.
49. Mirian N. Sotto, Berilo Langer, Sumie Hoshino-Shimizu, and Thales de Brito. Pathogenesis of Cutaneous Lesions in Acute Meningococcemia in Humans: Light, Immunofluorescent, and Electron Microscopic Studies of Skin Biopsy Specimens. *The Journal of Infectious Diseases*, 133(5):506–514, 05 1976. ISSN 0022-1899. doi: 10.1093/infdis/133.5.506.
50. Klaus Ley, Carlo Laudanna, Myron I. Cybulsky, and Sussan Nourshargh. Getting to the site of inflammation: the leukocyte adhesion cascade updated. *Nature Reviews Immunology*, 7 (9):678–689, Sep 2007. ISSN 1474-1741. doi: 10.1038/nri2156.
51. Manli Zhou, Yunfeng Yu, Ruiyi Chen, Xingci Liu, Yilei Hu, Zhiyan Ma, Lingwei Gao, Weixiong Jian, and Liping Wang. Wall shear stress and its role in atherosclerosis. *Frontiers in Cardiovascular Medicine*, 10, 2023. ISSN 2297-055X. doi: 10.3389/fcvm.2023.1083547.
52. Dorian Obino and Guillaume Dumenil. The many faces of bacterium-endothelium interactions during systemic infections. *Microbiology Spectrum*, 7(2):10.1128/microbiolspec.bai–0010–2019, 2019. doi: 10.1128/microbiolspec.bai-0010-2019.
53. H. H. T. Middelkamp, H. J. Weener, T. Gensheimer, K. Vermeul, L. E. de Heus, H. J. Albers, A. van den Berg, and A. D. van der Meer. Embedded macrophages induce intravascular coagulation in 3d blood vessel-on-chip. *Biomedical Microdevices*, 26(1):2, Dec 2023. ISSN 1572-8781. doi: 10.1007/s10544-023-00684-w.
54. Rory K. M. Long, François Korbmacher, Paolo Ronchi, Hannah Fleckenstein, Martin Schorb, Waleed Mirza, Mireia Mallorquí, Ruth Aguilar, Gemma Moncunill, Yannick Schwab, and Maria Bernabeu. Plasmodium falciparum impairs ang-1 secretion by pericytes in a 3d brain microvessel model. *bioRxiv*, 2025. doi: 10.1101/2024.03.29.587334.
55. Yuting Feng, Shuyi Wang, Xiaoye Liu, Yiming Han, Hongwei Xu, Xiaocen Duan, Wenyue Xie, Zhuoling Tian, Zuoying Yuan, Zhuo Wan, Liang Xu, Siying Qin, Kangmin He, and Jianyong Huang. Geometric constraint-triggered collagen expression mediates bacterial-host adhesion. *Nature Communications*, 14(1):8165, Dec 2023. ISSN 2041-1723. doi: 10.1038/s41467-023-43827-6.
56. Xiaoye Liu, Kui Zhu, Xiaocen Duan, Pudi Wang, Yiming Han, Wenjing Peng, and Jianyong Huang. Extracellular matrix stiffness modulates host-bacteria interactions and antibiotic therapy of bacterial internalization. *Biomaterials*, 277:121098, 2021. ISSN 0142-9612. doi: https://doi.org/10.1016/j.biomaterials.2021.121098.
57. Fenghua Zhao, Meng Zhang, Mehmet Nizamoglu, Hans J. Kaper, Linda A. Brouwer, Theo Borghuis, Janette K. Burgess, Martin C. Harmsen, and Prashant K. Sharma. Fibroblast alignment and matrix remodeling induced by a stiffness gradient in a skin-derived extracellular matrix hydrogel. *Acta Biomaterialia*, 182:67–80, 2024. ISSN 1742-7061. doi: https://doi.org/10.1016/j.actbio.2024.05.018.
58. Cristiane M. Franca, Maria Elisa Lima Verde, Alice Correa Silva-Sousa, Amin Mansoorifar, Avathamsa Athirasala, Ramesh Subbiah, Anthony Tahayeri, Mauricio Sousa, May Anny Fraga, Rahul M. Visalakshan, Aaron Doe, Keith Beadle, McKenna Finley, Emilios Dimitriadis, Jennifer Bays, Marina Uroz, Kenneth M. Yamada, Christopher Chen, and Luiz E. Bertassoni. Perivascular cells function as key mediators of mechanical and structural changes in vascular capillaries. *Science Advances*, 11(2):eadp3789, 2025. doi: 10.1126/sciadv.adp3789.
59. Anton Welker, Tom Cronenberg, Robert Zöllner, Claudia Meel, Katja Siewering, Niklas Bender, Marc Hennes, Enno R. Oldewurtel, and Berenike Maier. Molecular motors govern liquidlike ordering and fusion dynamics of bacterial colonies. *Phys. Rev. Lett.*, 121:118102, Sep 2018. doi: 10.1103/PhysRevLett.121.118102.
60. Lisa Craig, Katrina T. Forest, and Berenike Maier. Type iv pili: dynamics, biophysics and functional consequences. *Nature Reviews Microbiology*, 17(7):429–440, Jul 2019. ISSN 1740-1534. doi: 10.1038/s41579-019-0195-4.
61. Riya Joshi and Sunil D. Saroj. Survival and evasion of neisseria meningitidis from macrophages. *Medicine in Microecology*, 17:100087, 2023. ISSN 2590-0978. doi: https://doi.org/10.1016/j.medmic.2023.100087.
62. Md. Mominur Rahman, Fahadul Islam, Md. Harun Rashid, Abdullah Al Mamun, Saidur Rahaman, Mohaimenul Islam, Atkia Farzana Khan Meem, Popy Rani Sutradhar, Saikat Mitra, Anjuman Ara Mimi, Talha Bin Emran, Fatimawali, Rinaldi Idroes, Trina Ekawati Tallei, Muniruddin Ahmed, and Simona Cavalu. The gut microbiota (microbiome) in cardiovascular disease and its therapeutic regulation. *Frontiers in Cellular and Infection Microbiology*, 12, 2022. ISSN 2235-2988. doi: 10.3389/fcimb.2022.903570.
63. Camilla Urbaniak, Joanne Cummins, Muriel Brackstone, Jean M. Macklaim, Gregory B. Gloor, Chwanrow K. Baban, Leslie Scott, Deidre M. O'Hanlon, Jeremy P. Burton, Kevin P. Francis, Mark Tangney, and Gregor Reid. Microbiota of human breast tissue. *Applied and Environmental Microbiology*, 80(10):3007–3014, 2014. doi: 10.1128/AEM.00242-14.
64. Deborah Nejman, Ilana Livyatan, Garold Fuks, Nancy Gavert, Yaara Zwang, Leore T. Geller, Aviva Rotter-Maskowitz, Roi Weiser, Giuseppe Mallel, Elinor Gigi, Arnon Meltser, Gavin M. Douglas, Iris Kamer, Vancheswaran Gopalakrishnan, Tali Dadosh, Smadar Levin-Zaidman, Sofia Avnet, Tehila Atlan, Zachary A. Cooper, Reetakshi Arora, Alexandria P. Cogdill, Md Abdul Wadud Khan, Gabriel Ologun, Yuval Bussi, Adina Weinberger, Maya Lotan-Pompan, Ofra Golani, Gili Perry, Merav Rokah, Keren Bahar-Shany, Elisa A. Rozeman, Christian U. Blank, Anat Ronai, Ron Shaoul, Amnon Amit, Tatiana Dorfman, Ran Kremer, Zvi R. Cohen, Sagi Harnof, Tali Siegal, Einav Yehuda-Shnaidman, Einav Nili Gal-Yam, Hagit Shapira, Nicola Baldini, Morgan G. I. Langille, Alon Ben-Nun, Bella Kaufman, Aviram Nissan, Talia Golan, Maya Dadiani, Keren Levanon, Jair Bar, Shlomit Yust-Katz, Iris Barshack, Daniel S. Peeper, Dan J. Raz, Eran Segal, Jennifer A. Wargo, Judith Sandbank, Noam Shental, and Ravid Straussman. The human tumor microbiome is composed of tumor type–specific intracellular bacteria. *Science*, 368(6494):973–980, 2020. doi: 10.1126/science.aay9189.
65. Christopher Arakawa, Celina Gunnarsson, Caitlin Howard, Maria Bernabeu, Kiet Phong, Eric Yang, Cole A Deforest, Joseph D Smith, and Ying Zheng. Biophysical and biomolecular interactions of malaria-infected erythrocytes in engineered human capillaries. *Science Advances*, 2020.
66. Christophe Rusniok, David Vallenet, Stéphanie Floquet, Helen Ewles, Coralie Mouzé-Soulama, Daniel Brown, Aurélie Lajus, Carmen Buchrieser, Claudine Médigue, Philippe Glaser, and Vladimir Pelicic. Nemesys: a biological resource for narrowing the gap between sequence and function in the human pathogen neisseria meningitidis. *Genome Biology*, 10 (10):R110, Oct 2009. ISSN 1474-760X. doi: 10.1186/gb-2009-10-10-r110.
67. Xavier Nassif, Jonathan Lowy, Paula Stenberg, Peadar O'Gaora, Amir Ganji, and Magdalene So. Antigenic variation of pilin regulates adhesion of neisseria meningitidis to human epithelial cells. *Molecular Microbiology*, 8(4):719–725, 1993. doi: https://doi.org/10.1111/j.1365-2958.1993.tb01615.x.
68. DS Kellogg, IR Cohen, LC Norins, AL Schroeter, and G Reising. Neisseria gonorrhoeae. ii. colonial variation and pathogenicity during 35 months in vitro. *Journal of bacteriology*, 96 (3):596—605, September 1968. ISSN 0021-9193. doi: 10.1128/jb.96.3.596-605.1968.
69. Daphne Bindels, Lindsay Haarbosch, Laura van Weeren, Marten Postma, Katrin E. Wiese, Marieke Mastop, Sylvain Aumonier, Guillaume Gotthard, Antoine Royant, Mark A. Hink, and Theodorus W. J. Gadella Jr. mscarlet: a bright monomeric red fluorescent protein for cellular imaging. *Nature Methods*, 14:53–56, 2017. doi: https://doi.org/10.1038/nmeth.4074.
70. May Ho, Michael J. Hickey, Allan G. Murray, Graciela Andonegui, and Paul Kubes. Visualization of Plasmodium falciparum–Endothelium Interactions in Human Microvasculature: Mimicry of Leukocyte Recruitment. *Journal of Experimental Medicine*, 192(8):1205–1212, 10 2000. ISSN 0022-1007. doi: 10.1084/jem.192.8.1205.
71. Philippe Esterre, Amina Ait-Saadi, Laurence Arowas, Sophie Chaouche, Nicole Corre-Catelin, Christine Fanaud, Hélène Laude, Vesna Mellon, Valérie Monceaux, Gloria Morizot, Imène Najjar, Catherine Ottone, Blanca Liliana Perlaza, Blandine Rimbault, Linda Sangari, and Marie-Noëlle Ungeheuer. The icareb platform: A human biobank for the institut pasteur and beyond. *Open Journal of Bioresources*, 2020. doi: 10.5334/ojb.66.

Acknowledgments

We thank P. Vargas, A. Desys and M. Bernard (Leukomotion, Institut Necker Enfants Malades) for their help in the purification of human neutrophils and C. Travaillé (Photonic Bioimaging, Institut Pasteur) for complementary microfluidic chip imaging. We are grateful to the healthy volunteers of blood donation, for their participation in the study. We thank ICAReB-Clin of the Medical Direction and ICAReB-biobank of the CRBIP (BioResource Center) of the Institut Pas-teur (Paris) for providing blood samples from healthy volunteers. To H. Laude, L. Arowas, B. L. Perlaza, A. Z. M. Delhaye and C. Noury for managing the participants' visits. To E. Roux, R. Artus, L. Sangari, D. Cheval, S. Vacant, for preparing the blood samples from

donors.
Funding was obtained by GD from the Fondation pour la Recherche Médicale (EQU202203014610), the DESTOP European Research Council (ERC) Advanced grant, the Fondation NRJ, the 'Integrative Biology of Emerging Infectious Diseases' Labex (ANR 10-LBX-62 IBEID). Funding was obtained by GD and SG from the The Association Nationale pour la Recherche (ANR MeningoChip 18-CE15-0006-01) and the Région Ile-de-France (program DIM1HEALTH). This work was also supported by DIM ELICIT's grant from Région Ile-de-France, obatined by SG.

Author contributions

LP performed all the *in vitro* experiments. LP and JWN performed the material characterization. PN conducted all *in vivo* experiments, with LP handling the related analyses. JWN and TTN developed the photoablation system. EF designed the microfluidic chip. LP and VP carried out the experiments involving neutrophils. SGou created all the bacterial strains. MC, CB and DO contributed to the initial development of the chip. LP, DO, SGob, and GD conceived the project and secured funding. LP and GD wrote the article. All authors proofread and agreed on the manuscript.

Competing interest statement

The authors declare that they have no known competing financial interests.

Methods and Materials

Bacteria strains and culture. Infections were performed using *N. meningitidis* strains derived from the 8013 serogroup C strain (http://www.genoscope.cns.fr/agc/nemesys) (66). Mutations in *pilD* gene have been previously described (66). Wild-type and *pilD* bacterial strains were genetically modified to constitutively express either the green fluorescent protein (GFP) (13), the mScarlet fluorescent protein (mScar), or the near-infrared fluorescent protein (iRFP) under the control of the pilE gene promoter (9).
Strains were streaked from -80°C freezer stock onto GCB agar plates and grown overnight (5% CO_2, 37°C). For all experiments, bacteria were transferred to liquid cultures in pre-warmed RPMI-1640 medium (Gibco) supplemented with 10% FBS at adjusted OD_{600nm} = 0.05 and incubated with gentle agitation for 2h at 37°C in the presence of 5% CO_2.

Bacterial strains and growth conditions. *Neisseria meningitidis* 8013 serogroup C strain was used in the previous study (67). Bacteria were grown on Gonococcus Medium Base (GCB, Difco) agar plates supplemented with Kellogg's supplements (68) and antibiotics when required (5 µg/ml chloramphenicol), at 37°C in a moist atmosphere containing 5% CO_2.
Escherichia coli transformants were grown at 37°C on liquid or solid Luria-Bertani medium (Difco) containing 50µg/ml kanamycin (for pCR-Blunt II-TOPO plasmid) or 20µg/ml chloramphenicol plus 100 µg/ml ampicillin (for pMGC5-derived plasmid).

pMGC24 construct. A plasmid allowing stable expression of the mScarlet-I fluorescent protein (69) in *Neisseria meningitidis*, pMGC24, was constructed as follows: the sequence encoding the mScarlet-I fluorescent protein was PCR-amplified from the plasmid pmScarlet-I-C1 (Addgene #85044) with PacI and XhoI restriction sites in 5' and 3' respectively using the following primers: PacI_mScar_F: **TTAATTAA***AGGAGTAATTTT*ATGGTGAGCAAGGGCGAG and XhoI_mScar_R: **CTCGAG**TTACTTGTACAGCT CGTCCATGC (with restriction sites **bolded** and RBS of *pilE* in *italic*). The PCR fragment was then cloned into the pCR-Blunt II-TOPO vector (Invitrogen). After sequencing of the insert, the plasmid was cut with PacI and XhoI, and the resulting fragment was ligated to PacI/XhoI- linearized pMGC5 plasmid (15) that allows homologous recombination at an intergenic locus of the *Nm* chromosome and expression under the control of the constitutive *pilE* promoter.

Chips production. The microfluidic chip was designed on Clewin™ 5.4 (WieWeb software). The corresponding photolithography mask was ordered from Micro Lithography Services LTD (Chelmsford, UK). The chip molds were created by means of photolithography on an MJB4 mask aligner (Süss MicroTec, Germany). Briefly, SUEX-K200 resin (DJ Microlaminates Inc., US) was laminated onto a 4-inch silicon wafer. Lamination temperature, baking, UV exposure dose, and development steps were performed according to the manufacturer's recommendations to produce molds with a 200 µm height. Obtained heights were verified with a contact profiler (DektakXT, Bruker). After overnight silanization, (Trichloro(1H,1H,2H,2H-perfluorooctyl)silane, Sigma-Aldrich) replication of the devices was performed with polydimethyl-siloxane (PDMS, Silgard 184; Dow Chemical). After polymerization, PDMS slabs were cut and punched to form inlets and outlets (1 and/or 4 mm^2 for lateral channels, 1 mm^2 for central channel). Bonding onto glass-bottom ibidi dishes (Ibidi, #81158) was performed with a Cute plasma cleaner (Femto science, Kr). Critically, assembled microfluidic chips were heated at 80ºC for 48h to ensure both robust bonding and nominal PDMS hydrophobicity to allow consecutive hydrogel loading.
Chips were cooled down at 4°C for at least 8 hours to avoid quick polymerization while introducing the hydrogel in the chip. The collagen I solution was introduced in the center channel (see Fig. 1). FujiFilm collagen I (LabChem Wako, Collagen-Gel Culturing Kit) has been used to ob-

tain the 2.4 mg/ml solution, while the high concentration collagen I (Corning, #354249) has been used to obtain the 6 mg/ml, 4 mg/ml, and 3.5 mg/ml solutions according to the manufacturer's protocol. After collagen polymerization at 37°C for 20 min, PBS (Gibco) was added to the chips via the large lateral channels to avoid hydrogel drying. The inlet and outlet of the hydrogel channel were blocked with a droplet of liquid PDMS. Finally, chips were incubated at 37°C for several hours to complete the hydrogel polymerization.

The collagen I matrix was carved using a pulsed UV-laser (MOPA-355, 500 mW) focused through a 20x objective with NA=0.7 (UCPLFLN20X). The chip was then displaced with the microscope stage (SCANPLUS-IM, Marzhauser Wetzlar) at 1 mm/s to control the ablation region. Laser intensity was checked before each experiment using a light sensor (Thorlabs, Power sensor head S170C, and Power Meter for Laser, PM100A). Laser power under the sample was adjusted at 10 mW. The geometries of vessels have been designed with FUSION 360 (AutoCAD) or extracted from intravital microscopy images, exported on a .png binary image, and imported in a python code. The control of the various elements is embedded and checked for this specific set of hardware. The code is available upon request. Notably, photoablation is a homemade fabrication technique that can be implemented in any lab dotted with an epifluorescence microscope.

Of note, Corning collagen gels above 6 mg/ml have not been assessed in VoC because are too viscous and leak from the center channel, and those below 3.5 mg/ml are too liquid to be UV-carved (mechanically unstable). Also, a too-high energy alters collagen by forming cavitation bubbles that degrade the scaffold edges, while a too-thin tube will avoid the entry of cells, both making impossible use of the VoC.

Cell culture, Vessel-on-Chip production, and experiments. Primary human umbilical endothelial cells (HUVECs) were purchased from Lonza (pooled donors, #C2519A) and cultured in EGM-2 complete medium (Lonza, #CC-3162) in untreated 75 cm^2 flasks – 37°C, 5% CO_2. Cells were used between passages 2 and 6. Before passage or chip endothelialization, HUVEC were detached with 3 mL of Trypsin/EDTA (Gibco) for 4 min at RT. The cell/Trypsin/EDTA suspension was diluted with 4 mL of EGM-2 medium and centrifugated for 5 min at 1200 RPM (i.e. 300 G). After supernatant removal, the cell pallet is diluted at 1/3 for passage and concentrated at 14 x10^6 cells/mL for chip endothelialization.

Before endothelialization, chips were washed twice with a warm EGM-2 (with antibiotics) culture medium. The medium was partially removed (to avoid bubbles in the system) and 5 µl of the 14M cells/mL suspension were introduced in the chip via one lateral channel (see Fig.1). Chips were then incubated for 30 min at 37°C and 5% CO_2. The same operation was repeated for the other lateral channel. After 30 more min of incubation, chips were gently washed with EGM-2 medium (with antibiotics) to remove non-adherent cells. Chips were kept at 37°C and 5% CO_2 for 12h.

The flow was added to the setup 12h after cell seeding: syringes (SGE, 2.5 mL, glass) were connected to the chips (needle: SGE^{TM} Gastight Syringes, tubings: Tygon – Saint-Gobain, ID 0.02 mm and OD 0.06 mm / PTFE - Merck) and controlled via a syringe-pump (Cetoni). Microfluidic chips were kept at 37°C - 5% CO_2 for at least 24h.

For TNFα treatment, a solution of 50 ng/mL (Sigma, #H8916) has been introduced in chips for 4h (37°C, 5% CO_2) to induce inflammation on the endothelium.

For bacterial infection, Vessel-on-Chips were rinsed 3 times with EGM-2 (without antibiotics) and kept at 37°C and 5% CO_2 overnight. After 2h of gentle agitation in EGM-2 (without antibiotics) culture medium as explained above, 10 µl of bacteria solution OD_{600nm} = 0.05 are introduced in the Vessel-on-Chip. Flow was added to the setup following the description as above explained, during the 3h of infection, with a flow rate of 0.5 µl/min.

Mice. SCID/Beige (CB17.Cg-PrkdcscidLystbg-J/Crl) mice were used in all the experiments (Central Animal Facility, Institut Pasteur, Paris, France). Mice were housed under the specific pathogen-free condition at Institut Pasteur. Mice were kept under standard conditions (light 7 am - 7 pm; temperature 22 $\pm$ 1°C; humidity 50 $\pm$ 10%) and received sterilized rodent feed and water *ad libitum*. All experiments were performed in agreement with guidelines established by the French and European regulations for the care and use of laboratory animals and approved by the Institut Pasteur Committee on Animal Welfare (CETEA) under the protocol code CETEA 2018-0022. For all experiments, male and female mice between 6 and 13 weeks of age were used. Littermates were randomly assigned to experimental groups.

Xenograft model of infection preparation. Five to eight weeks old mice, both males and females, were grafted with human skin as previously described (7). Briefly, a graft bed of about 1 cm^2 was prepared on the flank of anesthetized mice (intraperitoneal injection of ketamine and xylazine at 100 mg/kg and 8.5 mg/kg, respectively) by removing the mouse epithelium and the upper dermis layer. A 200-µm thick human skin graft comprising the human epidermis and the papillary dermis was immediately placed over the graft bed. Grafts were fixed in place with surgical glue (Vetbond, 3 M, USA) and dressings were applied for 1 week. Grafted mice were used for experimentation 4-10 weeks post-surgery when the human dermal microvasculature is anastomosed to the mouse circulation without evidence of local inflammation, as previously described (7).

Normal human skin was obtained from adult patients (20-60 years old), both males and females, undergoing plastic surgery in the service de *Chirurgie Reconstructrice*

et Plastique of Groupe Hospitalier Saint Joseph (Paris, France). In accordance with the French legislation, patients were informed and did not refuse to participate in the study. All procedures were approved by the local ethical committee Comité d'Evaluation Ethique de l'INSERM IRB 00003888 FWA 00005881, Paris, France Opinion: 11048. Then, intravital imaging of the human xenograft was adapted from (70). Briefly, 30-min prior to surgery, mice were injected subcutaneously with buprenorphine (0.05 mg/kg) and anesthetized by spontaneous inhalation of isoflurane in 100% oxygen (induction: 4%; maintenance: 1.5% at 0.3 L/min). A middle dorsal incision was made from the neck to the lower back and the skin supporting the human xenograft was flipped and secured onto an aluminum custom-made heated deck at 36°C. The human microvasculature within the graft was exposed by carefully removing the excess of connective tissue. The skin flap was covered with a coverslip and maintained thanks to a 3D-printed custom-made holder to avoid any pressure on the xenograft vasculature, sealed with vacuum grease, and continuously moistened with warmed 1× PBS (36°C). Mice hydration was maintained by intraperitoneal injection of 200 µl 0.9% saline solution every hour. During the experiment, the mouse's body temperature was maintained at 37°C using a heating pad. The tail vein was cannulated allowing the injection of fluorescent dyes and/or bacteria. In all experiments, human vessels were labeled using fluorescent conjugated UEA-1 lectin (100 µg, Dylight 650 or Dylight755, Vector Laboratories), and five to ten fields of view of interest containing human vessels were selected per animal for observations.

Ear mice preparation. Mice were anesthetized by spontaneous inhalation of isoflurane in 100% oxygen (induction: 4%; maintenance: 1.5% at 0.3 l/min) and placed in ventral decubitus on a heating pad (37℃) to maintain body temperature. The dorsal face of the ear pinnae was epilated using depilatory cream without causing irritation. The ear was carefully flattened out on an aluminum custom-made heated deck at 36℃ and held in place with a coverslip. The tail vein was cannulated allowing the injection of fluorescent dyes.

Immunostaining. Collagen gels have been stained with a Maleimide Alexa Fluor™ 488 (ThermoFisher, #A10254) solution: 10 µl of Maleimide (100 µg/ml) has been diluted within 700 µl of a 0.2 M sodium bicarbonate buffer solution. Chips were incubated with this solution for 1h at RT in the dark, and finally gently washed with PBS before imaging.
For E-selectin experiments, before and after TNFα treatment or bacterial infection, a solution of 10^{-3} mg/ml PE-conjugated anti-human E-selectin (CD62E clone P2H3, Thermofisher Scientific, #12-0627-42) has been introduced in the chips to stain the endothelium for 10 min. After gentle washing steps with EGM-2 medium, E-selectin expression was acquired (Nikon, Spinning disk, Obj. 20X, dry, NA=0.75).
Chips were fixed with PFA 4%v/v in PBS for 15 min, permeabilized with Triton X-100 1%v/v in PBS for 30 min, blocked with PBS-gelatin 1%v/v in PBS for 15 min, and mounted with fluoromount-G solution (Fluoromount-G, SouthernBiotech, #0100-01). Chips were incubated with Phalloidin at 0.66 µM (Alexa Fluor 488, Thermofisher, #A12379), anti-human PECAM antibody at 2.5 x10^{-3} mg/ml (Ultra-LEAF™ Purified anti-human CD31 Antibody, Biolegend #303143 - conjugated with DyLight Antibody Labeling Kits, Termofisher #53044), anti-human collagen IV antibody at 10^{-2} mg/ml (Alexa Fluor 642, Clone 1042, eBioscience #51-9871-82), rabbit anti-VE-cadherin (Abcam #ab33168) for 10h at 4°C. Alexa Fluor 555-conjugated donkey anti-rabbit antibody (Abcam #ab150074) and Hoechst 10^{-2} mg/ml (33362 trihydrochloride trihydrate, Invitrogen #H3570) has been added to the chips after 3 washing steps with PBS 1X, for 1h at room temperature.
Human and mice skin samples were fixed with PFA 4%v/v in PBS overnight, washed 3 times in PBS 1X (30 min of incubation time for each side), and blocked with buffer (0,3% triton + 1% BSA + 1% NGS in PBS) overnight at 4°C. Samples were stained for 3 days at 4°C with phalloidin (0.66 µM, Alexa Fluor 488, Thermofisher, #A12379) and overnight at 4°C with DAPI (0.3 mg/ml, ThermoFisher, #62247). A sample clear was made with a Rapid clear 1.47 medium for 2 days at room temperature and a mounting solution was introduced between slide and cover-slide in rapid clear medium.

Permeability assays. In VoC, 10 µl of a 0.1 mg/mL dextran solution (FITC, Sigma) have been introduced in chips during 30 min. Stacks of 4 images, spaced 1 µm apart, were acquired every minute.
In vivo, mice were intravenously injected with 20 µg of anti-mouse CD31 antibodies coupled with Alexa Fluor 647 (clone 390, Biolegend) to label blood vessels and the ear was allowed to stabilize for 30 min. Prior to imaging, 5 mg of fluorescein isothiocyanate (FITC) conjugated 70 kDa or 150 kDa dextran (Sigma-Aldrich, St Louis, MO) dissolved in 200 ml of phosphate-buffered saline (PBS) were injected intravenously. Stacks of 10 images, spaced 4 µm apart, were acquired every minute.
For both models, the permeability has been quantified following the equation:

$$P = \frac{R}{2}\frac{1}{\Delta I_0^{channel}}\frac{dI^{collagen}}{dt}$$

Where R is the channel radius, $\Delta I_0^{channel}$ the first step in increase of fluorescence in the vessel, and $dI^{collagen}/dt$ the rate of increase in fluorescence outside the vessel.
Image analysis was conducted over the first 8 minutes following the initial fluorescence increase within the lumen for both *in vivo* and VoC models, while the entire acquisition lasted more than 30 min. For each condition, the mean fluorescence intensity was measured inside the vessel and

in the surrounding area (background), both before and after introducing fluorescent Dextran. Due to reproducibility constraints in the animal model, only vessels without overlapping background vessels were included in the analysis.

Imaging Particle Image Velocimetry (PIV) and *in vivo* Wall Shear Stress (WSS). *In vivo*, basal microvascular blood flow in human vessels (arterioles and venules) was measured by high-speed acquisitions on a single plane (50 frames per second, 300 frames) of intravenously perfused (15 µl/min) 1 µm large fluorescent microspheres (Yellow/Green Fluoresbrite carboxylate, Polysciences, 107 microspheres/ml 1X PBS). Speed was determined from the centerline microsphere. The blood flow of each vessel was then computed from the vessel surface section and mean velocity following: $Q_{blood} = V_{bead}^{mean}.S_{vessel}$.
According to the figure 2B, the flow rate Q depends on vessel size D as $1/D^3$ (the blue and red fitting curves are $1/x^3$). Therefore, we can compute the WSS (τ) within circular structures following the equation 1:

$$\tau = \frac{4\eta}{\pi}\frac{Q}{R^3} \quad \textbf{(1)}$$

where R is the vessel radius, and the viscosity η of blood vessel between 25 and 100 µm is considered as constant (34) (η = 3.5 x10^{-3} Pa.s at 37°C). The WSS can be then averaged per vessel type (arterioles vs. venules) according to the equation Eq. (1). The same equation was used to compute the WSS in the Vessel-on-Chip from the flow rate Q.

Neutrophil adhesion and phagocytosis. For experiments in the VoC, human neutrophils have been purified from donor blood. Human peripheral blood samples were collected from healthy volunteers through the ICAReB-Clin (Clinical Investigation platform) of the Institute Pasteur (71). All participants received oral and written information about the research and gave written informed consent in the frame of the healthy volunteers CoSImmGEn cohort (Clinical trials NCT 03925272), after approval of the CPP Ile-de-France I Ethics Committee (2011, Jan 18th) (71). Neutrophils have been stained for nucleus (Hoechst, 10-3 mg/ml, 33362 trihydrochloride trihydrate, Invitrogen #H3570)) and actin (SPY555-actin, 1/1000, Spirochrome #CY-SC202). After 10 min of a TNFα-induced activation (10 ng/mL), 10 µl of a 6 M cells/mL suspension was introduced in the chips under flow. After, the flow has been added to the system at 0.7-1 µl/min. Human neutrophil adhesion and phagocytosis have been acquired within 1h at 37ºC and 5% CO_2.
In the animal model, after 2h of liquid culture, bacteria were washed twice in PBS and resuspended to 10^8 CFU ml^{-1} in PBS. Before infection, mice were injected intraperitoneally with 8 mg of human transferrin (Sigma Aldrich) to promote bacterial growth *in vivo*, as previously described (66) and neutrophils were labeled by were labeled with 2.5 µg Dylight550-conjugated anti-mouse Ly-6G (LEAF purified anti-mouse Ly-6G, clone 1A8, Biolegend, #127620 with DyLight550 Antibody Labelling Kit, ThermoFisher Scientific, #84530). Mice were infected by intravenous injection of 100 µl of the bacterial inoculum (10^7 CFU total) and time-lapse z-stack series (2-2.5 µm z-step, 50-80 µm range) were captured every 20 min for 3 hours to image bacterial growth and every 30 sec for 20 min to image phagocytosis of bacteria by neutrophils.

Rheology assays. Collagen gel viscoelastic properties were measured using an Ultra+ rheometer (Kinexus). 200 µl of collagen gel was placed at the center of the rheometer plate kept at 4°C plate. The 20 mm-diameter testing geometry was lowered to a gap of 200 µm. Excess of hydrogel was removed. Temperature was ramped up to 37°C (within 60 sec) to initiate the hydrogel formation. Gelation dynamics and gel properties were extracted from continuous geometry rotation at 1 Hz frequency and a 1% strain. Rheological values i.e. elastic modulus G' stabilized after 200 sec. Final values were determined by averaging values between 500 and 700 sec.

Actin fiber alignment/nucleus alignment and elongation. The z projection (Maximum Intensity) of the top and bottom parts of vessels have been realized for actin fibers and nucleus segmentation and analysis. Only the images taken with Leica Spinning disk microscope, 40X, NA=1.10 (see below for more details) were used for analyses. The fibers and the nuclei located at the vessel edges have been excluded from the analysis. The angle and the ratio major/minor axis have been measured for all vessels (circular plots) and averaged by vessel (dotted graph).
For *in vivo* images, the segmentation of nuclei has been achieved by hand for several z-slices for each vessel. The alignment (angle) and elongation (ratio major/minor) have been measured for all vessels (circular plots) and averaged by vessel (dotted graph).

***In vitro* actin recruitment and coherency.** The z projection (Maximum Intensity) of the top and bottom parts of the vessel (taken with the 40X, NA=1.10 - see below for more details) have been used to quantify actin recruitment and fibers coherency. Region of Interest (ROIs) of similar sizes were located on infected and non-infected areas of the endothelium. For each ROI, the mean fluorescence intensity has been subtracted by the background intensity (collagen matrix) and normalized by the mean of non-infected areas intensity:

$$I_{actinrecruitment} = \frac{I_{ROI}^{infected} - I_{background}}{mean(I_{ROI}^{non-infected})}$$

The coherency has been assessed with the OrientationJ Measure plugin (BIG, EPFL).

Simulations. The shear stress simulations have been performed with COMSOL Multiphysics 6.3. For each vessel, the contour has been segmented with Fiji ImageJ (ImageJ2, version 2.16.0/1.54g, 26d66057dd), transformed in binary image and saved in vectorial image (dxf) with Inskape (Inkscape 1.4, e7c3feb1, 2024-10-09). The dxf file has been used to produce the 2D fluid simulation in COMSOL.

Statistics. Post-processing and statistics analyses have been realized with R (R Studio version 2022.12.0+353, R version 4.2.2 (2022-10-31)). No statistical method was used to predetermine the sample size. Statistical tests were based on the Wilcoxon or t-tests – with p-values > 0.05: n.s., 0.05 < p-values < 0.01: *, 0.01 < p-values < 0.005: **, 0.005 < p-values < 0.001: ***, p-values < 0.001: ****. Scatter dot plots show the mean $\pm$ sd. Statistical details of experiments such as sample size, replicate number, and statistical significance, are explicitly added in the figure legends, and source data files.

Figures

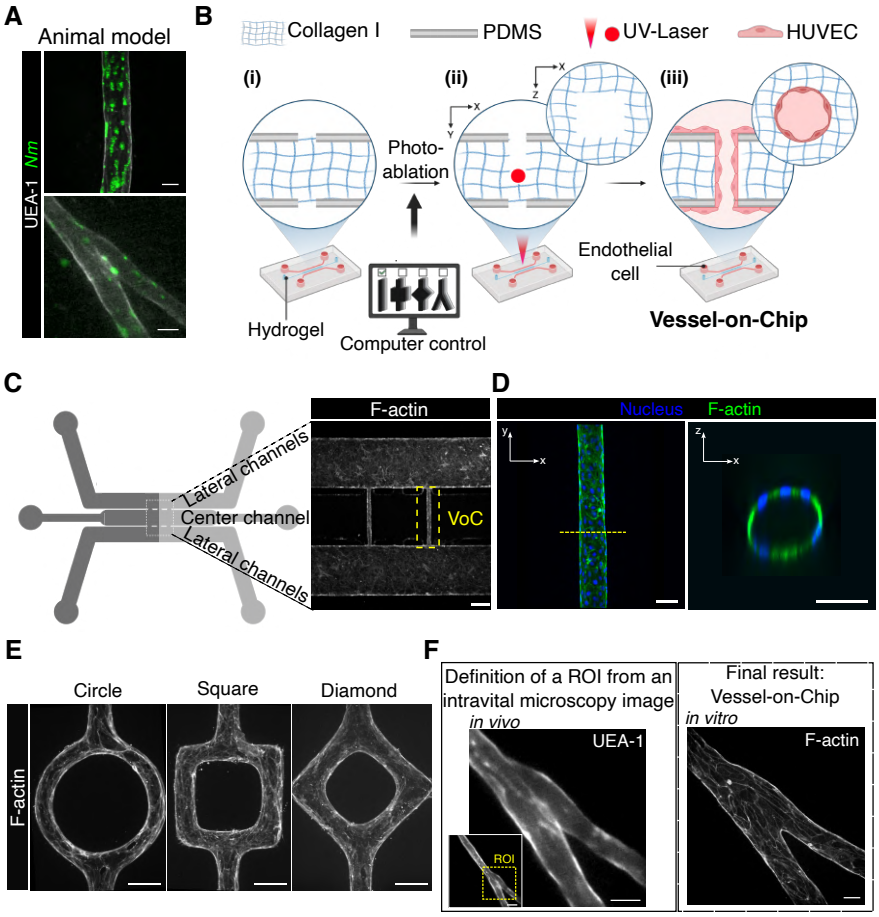

Fig. 1. Replicating the geometries of infected *in vivo* vessels using photoablation. (A) Confocal images of *Nm*-infected vessels in the human-skin xenograft mouse model. Scale bar: 25 µm. (B) Schematic representation of the development of the Vessel-on-Chip (VoC) device: (i) a collagen-based hydrogel is loaded in the center channel of the microfluidic device, (ii) the focused UV-laser locally carves the chosen geometry within the collagen I matrix, (iii) HUVEC are seeded and attach on the collagen-carved scaffold. (C) Schematic representation of the microfluidic device and zoom of the carved region after cell seeding (F-actin). Scale bar: 250 µm. (D) Confocal images of F-actin and related orthogonal view of the tissue-engineering VoC. Scale bar: 50 µm. (E) Confocal images of VoC in circle-, square- and diamond-shaped structures. Scale bar: 50 µm. (F) Photoablation process to create *in vivo*-like structures. Definition of the region of interest (ROI) to replicate from intravital microscopy images (left), and the obtained *in vivo*-like structures in the VoC (right). Scale bars: 20 µm.

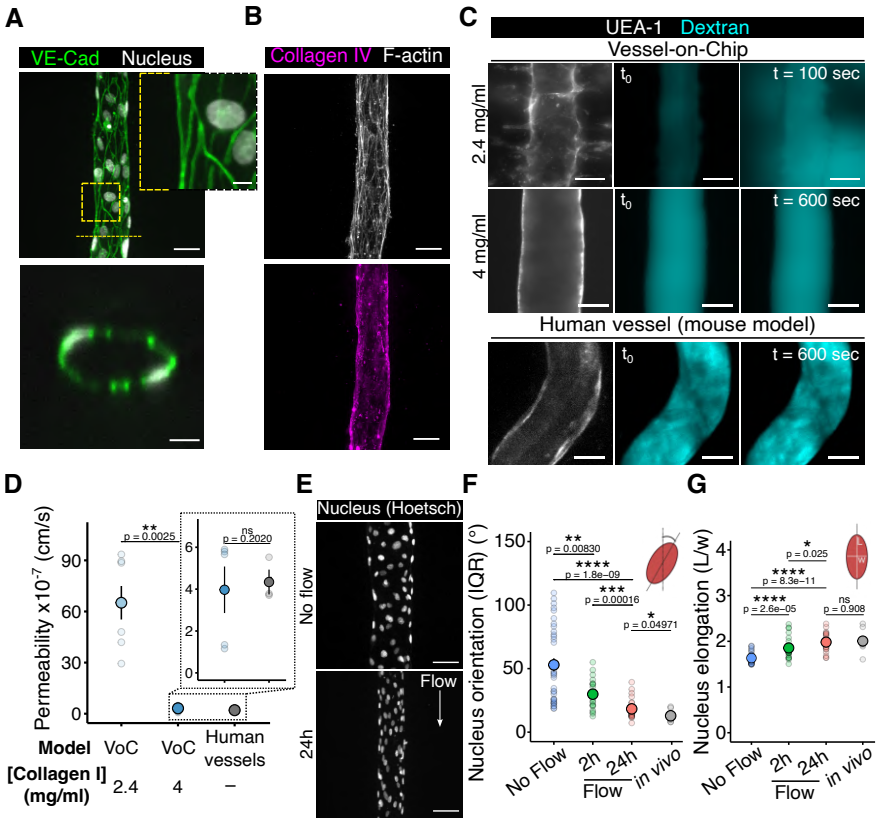

Fig. 2. The Vessel-on-Chip device provides nuclear morphologies under flow conditions and permeability levels similar to those observed *in vivo*. (A) Confocal images of the VE-Cadherin staining and (B) Collagen IV in the VoC. Scale bars: 50 µm (large view) and 7 µm (zoom). (C) Representative confocal images of fluorescent 150 kDa-Dextran (FITC) in the VoC (top, scale bar: 50 µm) and in the human vessel in the mouse model (bottom, scale bar: 30 µm). Fluorescence of the outside and inside regions of the vascular lumen has been measured to determine permeability. (D) Graph representing the permeability to 150 kDa-Dextran. Each dot represents one vessel. For each condition, the mean ± s.d. is represented (VoC, 2.4 mg/ml: 65.12 ± 26.00 cm/s (n=7) – VoC, 4 mg/ml: 3.97 ± 2.49 cm/s (n=5) - Human vessel *in vivo*: 8.00 ± 2.52 cm/s (n=7)). (E) Representative images of nucleus alignment in the absence and presence of flow (24h). Scale bar: 50 µm. (F-G) Graphs of nucleus orientation (IRQ: interquartile range) and elongation. Each dot corresponds to the mean value of one vessel. For each condition, the mean ± s.d. is represented (No flow: 53.0 ± 30.2° and 1.63 ± 0.11 a.u. (n=34) – 2h of flow: 29.9 ± 11.5° and 1.85 ± 0.25 a.u. (n=22) – 24h of flow: 18.2 ± 7.61° and 1.98 ± 0.20 a.u. (n=25) – *in vivo*: 12.9 ± 4.6° and 2.01 ± 0.23 a.u. (n=9)). All statistics have been computed with Wilcoxon tests.

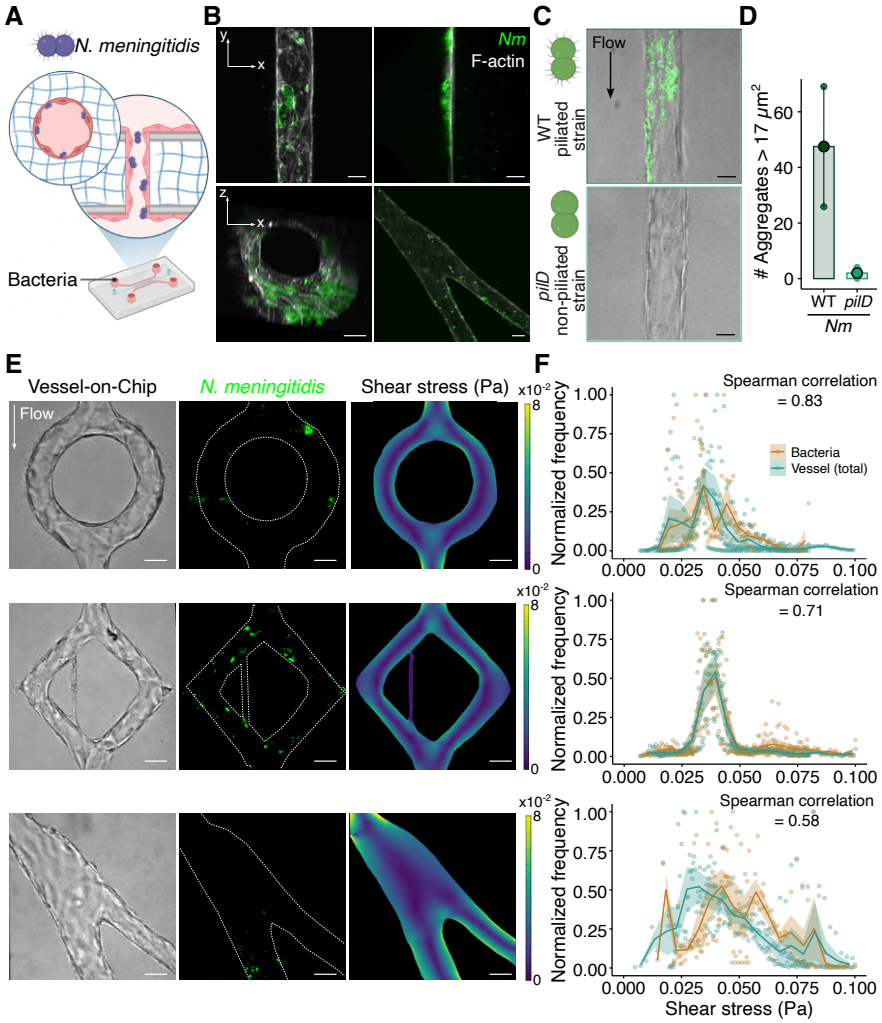

Fig. 3. *Neisseria meningitidis* adhesion to the Vessel-on-Chip device. (A) Schematic of the infected Vessel-on-Chip device. (B) Confocal images of infected vessels in our system 3h post-infection in each condition. Scale bar: 20 µm. (C) Bright-field and fluorescence confocal images of the VoC 3h post-infection with WT (top) and *pilD* (bottom) *Nm* strains. Scale bar: 25 µm. (D) Graph representing the number of aggregates 3h post-infection, with WT and *pilD Nm* strains. 17 μm^2 represents the median over the entire population of aggregate sizes. Each dot corresponds to a vessel. For each condition, the mean ± s.d. is represented (WT: 47.5 ± 30.4 (n=2) – *pilD*: 2.0 ± 2.0 (n=3)). (E) Brighfield (left) and fluorescence (center) images of the infected vessels of different designs (circle, diamond, *in vivo*-like) and related simulation of shear stress. Scale bar: 50 µm. (F) Normalized histograms of total (blue) and bacteria pixels (orange) depending on the shear stress values for each vessel design (from top to bottom, circle, diamond, *in vivo*-like). Solid curves represent the mean ± sd (n=3 experiments). Spearman correlation give the correlation between the mean curves.

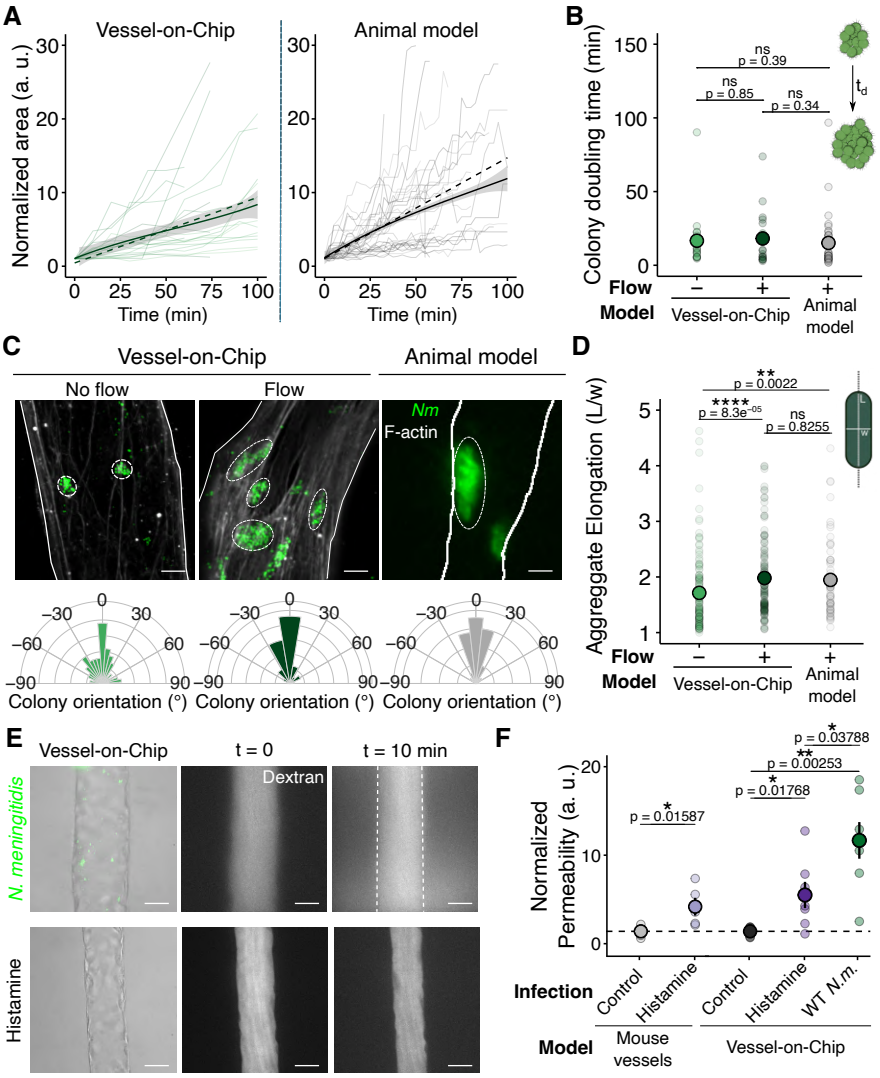

Fig. 4. Flow impacts colony morphology but not growth in both Vessel-on-Chip and animal models, and *Neisseria meningitidis* infection increases permeability in Vessel-on-Chip. (A) Normalized surface area of microcolonies over time, in the VoC under flow conditions (left, n=20) and in human vessels of the xenografted mouse model (right, n=33). Solid thin curves, solid thick curves, and dashed thick curves represent individual colony growth, mean, and linear fit (y = ax + 1), respectively. (B) Colony doubling time extracted from the curves (t_d=1/a). Each dot corresponds to a bacterial microcolony. For each condition, the mean ± s.d. is represented (VoC, Flow$^-$: 16.7 ± 18.5 min (n=21) — VoC, Flow$^+$: 26.2 ± 40.4 min (n=20) — *in vivo*: 15.2 ± 18.8 min (n=33)). (C) Confocal images of WT *Nm* microcolonies formed on the vascular wall 3h post-infection, in the absence and presence of flow (VoC), and in the animal model. Scale bar: 10 µm. Circular plots representing the distribution of microcolony orientation. (D) Graph representing the elongation of microcolonies 3h post-infection in each condition. Each dot corresponds to a microcolony. For each condition, the mean ± s.d. is represented (VoC, Flow$^-$: 1.75 ± 0.77 (n=128) — VoC, Flow$^+$: 2.11 ± 1.02 (n=125) — *in vivo*: 2.07 ± 0.971 (n=61)). (E) Brightfield and fluorescence confocal images of permeability assay (Dextran) in infected (top) and histamine-treated (bottom) Vessel-on-Chips. Scale bar: 25 µm. (F) Relative permeability values of VoC and *in vivo*, vessels treated with histamine and infected with *Nm*. Each dot represents a vessel. For each condition, the mean ± s.d. is represented (mouse vessel, Control: 1 ± 0.62 (n=5), Histamine: 3.79 ± 2.25 (n=5) — VoC, Control: 1 ± 0.63 (n=5), Histamine: 5.11 ± 3.92 (n=7), *Nm*: 11.3 ± 5.48 (n=7)). All statistics have been computed with Wilcoxon tests.

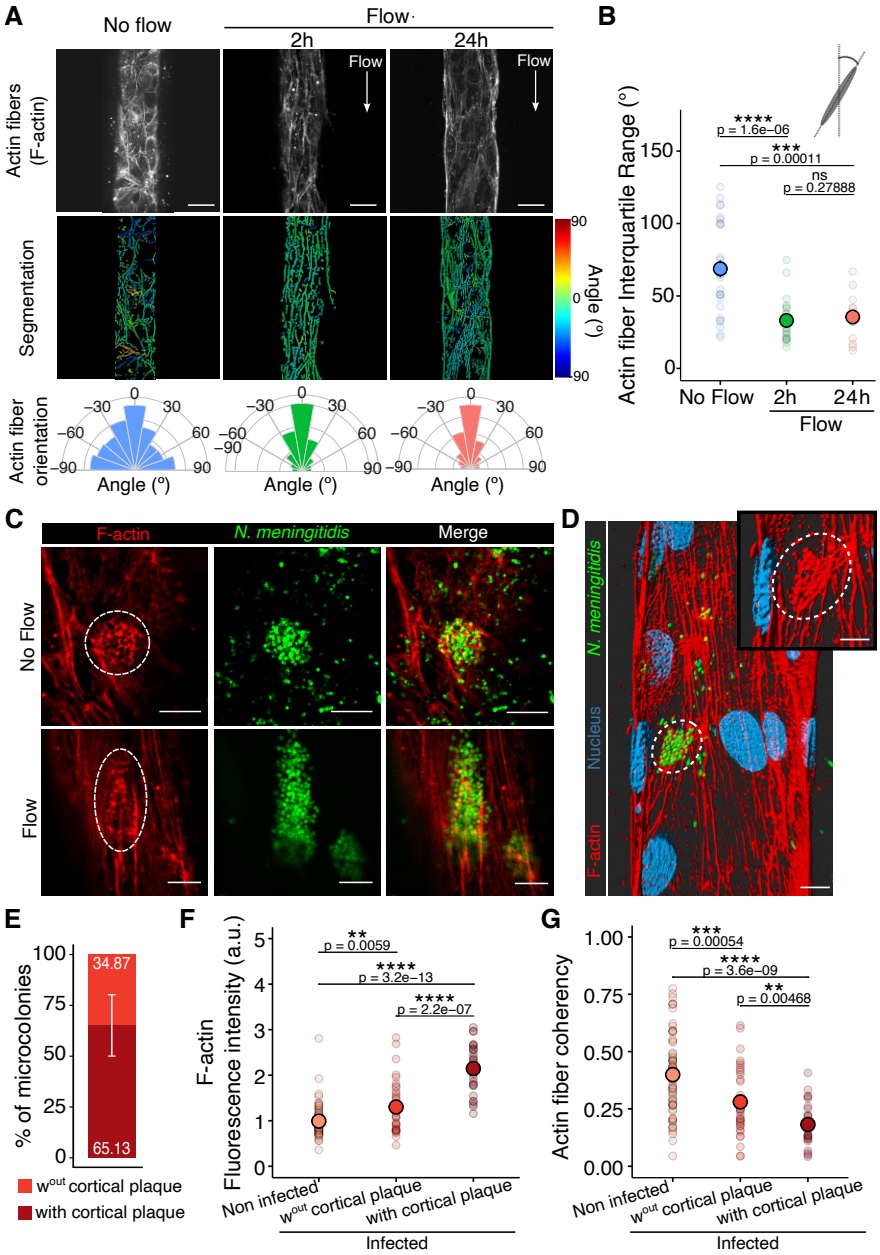

Fig. 5. Flow-induced aligned actin stress fibers are reorganized below bacterial microcolonies (A) Confocal images of the F-actin network in the VoC in the absence and presence of flow (2h and 24h) (top). Scale bar: 30 µm. Corresponding segmented images. The color code shows the alignment of the actin fibers with the direction of the flow (red to blue) (middle). Circular plots of the orientation distribution of actin fibers (bottom). (B) Interquartile range of F-actin fiber orientation. Each dot represents the mean of F-actin fiber orientation per vessel. For each condition, the mean ± s.d. is represented (No Flow: 68.8° ± 31.0° (n=29) — 2h of flow: 33.1° ± 14.3° (n=25) — 24h of flow: 35.5° ± 13.5° (n=19)). (C) Confocal images of honeycomb-shaped cortical plaque formed by *Nm* microcolonies in the absence (top) and presence of flow (bottom) in the VoC. Scale bar: 10 µm. (D) 3D rendering of a vessel infected with *Nm* 3h post-infection under flow conditions. Scale bar: 15 µm (main) and 10 µm (zoom). (E) Percentages of colonies forming a cortical plaque (n=5 vessels). (F) F-actin fluorescence intensity under each microcolony and on non-infected regions of the same area. Each dot represents a region of a microcolony. For each condition, the mean ± s.d. is represented (Not infected regions: 0.99 ± 0.33 a.u. (n=74) — Infection, without cortical plaque: 1.30 ± 0.57 a.u. (n=36) — Infection, with cortical plaque: 2.15 ± 0.54 a.u. (n=28)). (G) Coherency of F-actin fibers on non-infected regions and on infection sites. Each dot represents a colony. For each condition, the mean ± s.d. is represented (Not infected regions: 0.40 ± 0.17 a.u. (n=74) — Infection, without cortical plaque: 0.28 ± 0.15 a.u. (n=36) — Infection, with cortical plaque: 0.18 ± 0.09 a.u. (n=28)). All statistics have been computed with Wilcoxon tests.

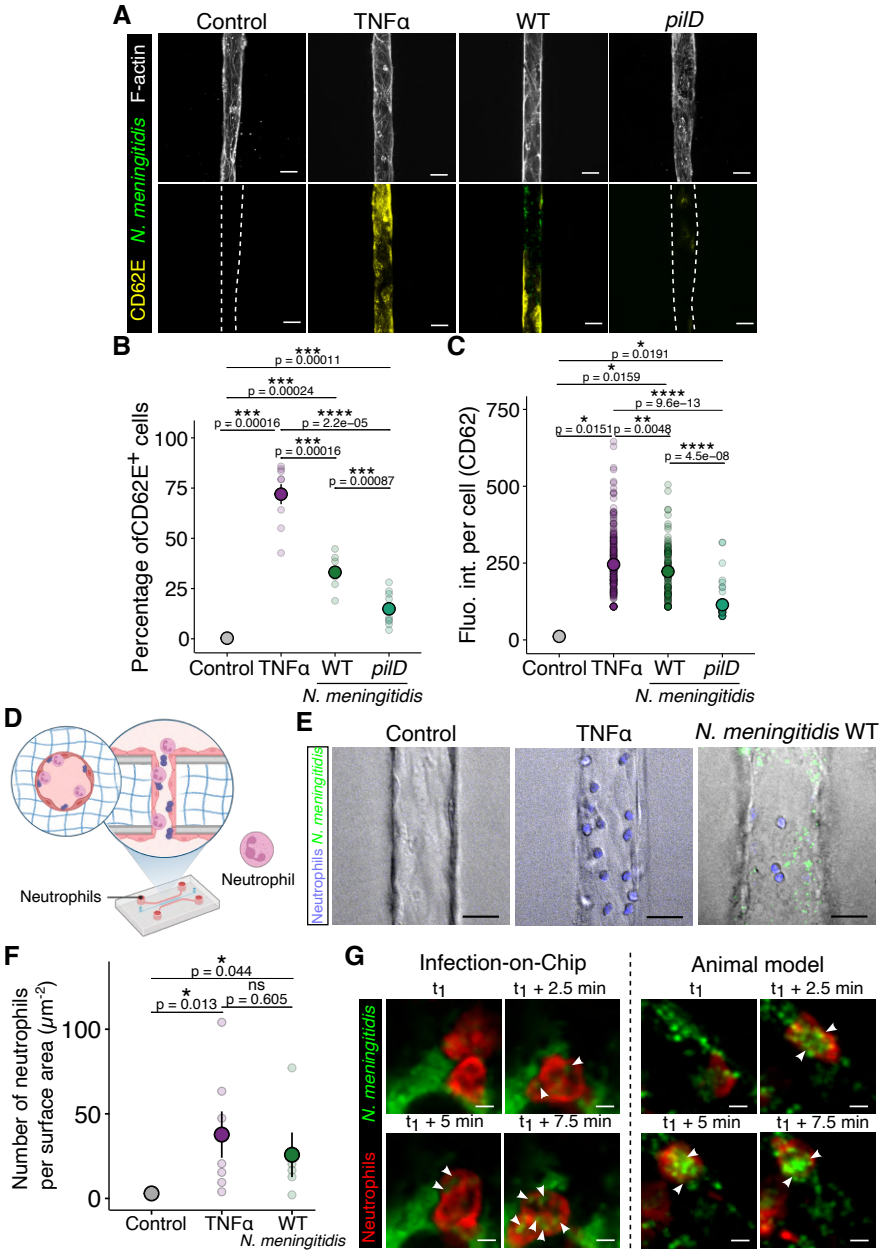

Fig. 6. The Our infection model recapitulates the human neutrophil response to *N. meningitidis* infection. (A) Confocal images of E-selectin staining in the VoC for four conditions: without infection nor treatment, after 4h of either TNFα treatment or infection with WT or *pilD Nm* strains. Scale bar: 50 µm. (B-C) Graphs representing the percentage of E-selectin positive cells and the mean intensity of CD62 in positive cells. For each condition, the mean ± s.d. is represented (Control: 0.32% ± 0.67% (n=10 vessels), 11.4 ± 1.17 (n=2 cells) — TNFα: 72.0% ± 15.0% (n=9 vessels), 245 ± 100 (n=244 cells) — WT: 33.1% ± 8.12% (n=8 vessels), 223 ± 118 (n=126 cells) — *pilD*: 14.9% ± 8.1% (n=10 vessels), 144 ± 58.4 (n=44 cells)). (D) Schematic representation of the setup. Purified neutrophils were introduced in the microfluidic chip under flow conditions (0.7-1 µl/min). (E) Bright-field and fluorescence images of neutrophils adhering on a non-treated (control), TNFα-treated, or *Nm*-infected VoC. Scale bar: 25 µm. (F) Graph representing the number of neutrophils adhering to the endothelium for each condition. Each dot represents a vessel. For each condition, the mean ± s.d. is represented (Control: 0.59 ± 1.32 µm^{-2} (n=5) — TNFα: 33.0 ± 36.1 µm^{-2} (n=8) — *N. meningitidis*: 21.5 ± 28.4 µm^{-2} (n=6)). (G) Representative images of bacteria phagocytosis by neutrophils in infected VoC (left) and in infected human vessels in the grafted mouse model (right). Scale bar: 25 µm. All statistics have been computed with Wilcoxon tests.